Aerospace Science and Technology 156 (2025) 109726

Contents lists available at ScienceDirect

Aerospace Science and Technology

journal homepage: www.elsevier.com/locate/aescte

Nonlinear guided waves in improved silicon solar cells using mathematical modeling and a bio-inspired artificial intelligence algorithm

Lei Chang [a], Wenqing Yang [a,*], Mohammed El-Meligy [b,c], Khalil El Hindi [d]

[a] School of Carbon Neutrality Science and Engineering, Anhui University of Science and Technology, Huainan, 232001, China
[b] Jadara University Research Center, Jadara University, PO Box 733, Irbid, Jordan
[c] Applied Science Research Center, Applied Science Private University, Amman, Jordan
[d] Department of Computer Science, College of Computer & Information Sciences, King Saud University, Riyadh 11543, Saudi Arabia

ARTICLE INFO

Communicated by Sirish Namilae

Keywords:
Nonlinear guided waves
Improved silicon solar cells
GPL nanocomposites
Bio-inspired artificial intelligence algorithm
Runge–Kutta method

ABSTRACT

Solar cells are crucial in aerospace industries as they provide a reliable and sustainable power source for spacecraft and satellites, enabling long-duration missions without relying on conventional fuel. This study investigates the propagation of nonlinear guided waves in improved silicon solar cells reinforced by graphene platelet (GPL) nanocomposites. The microplate model of the solar cells is developed using the modified couple stress theory (MCST) to capture size-dependent effects, and the sinusoidal shear deformation theory (SSDT) is applied to account for realistic shear deformation behavior. Nonlinear governing equations describing the dynamic response of the system are derived using Hamilton's principle. The equations are then solved numerically using the Runge–Kutta method to analyze the phase velocity and wave characteristics under varying parameters. The effects of GPL weight fraction, length scale parameter, and wavenumber on wave propagation are thoroughly examined. In this investigation, an intelligent model based on deep neural networks as an artificial intelligent algorithm combined with a genetic algorithm (DNN-GA) as a bio-inspired optimization approach, is employed to predict nonlinear phenomena in guided waves within the solar cell, using datasets generated from mathematical simulations. The results demonstrate that the inclusion of GPL nanocomposites enhances the mechanical properties of the silicon solar cells, leading to higher phase velocities and improved wave propagation efficiency. Additionally, the influence of the length scale parameter on phase velocity is found to be significant, particularly for low wavenumbers. This study provides valuable insights into the optimization of advanced nanocomposite-reinforced silicon solar cells for applications requiring efficient guided wave propagation. The findings offer a promising approach for the design and enhancement of next-generation solar cells.

1. Introduction

Solar cells are vital for the aerospace industry as they provide a continuous and renewable energy source, essential for the operation of satellites and spacecraft over extended periods [1,2]. Their ability to function efficiently in the vacuum of space, where traditional energy sources are impractical, makes them indispensable for powering systems like communication, navigation, and scientific instruments [3]. The high energy-to-weight ratio of solar cells reduces payload mass, contributing to more cost-effective and fuel-efficient launches [4]. Moreover, advances in solar cell technology have enabled longer mission durations, reducing the need for frequent maintenance or replacement of power sources in space [5].

Silicon solar cells are of great importance to engineers due to their high efficiency in converting sunlight into electrical energy, making them a widely used technology in renewable energy systems [6,7]. As one of the most mature and well-researched photovoltaic technologies, silicon solar cells offer a reliable and scalable solution for generating clean electricity [8]. Their long operational lifespan, often exceeding 25 years, provides engineers with a cost-effective energy source for large-scale projects, reducing the need for frequent replacements or repairs [9]. Silicon, being abundant in nature, ensures that these solar cells can be produced at a relatively low cost, supporting the widespread deployment of solar energy solutions [10]. Engineers also value silicon solar cells for their structural durability and ability to withstand various environmental conditions, including high temperatures and exposure to

* Corresponding author.
E-mail address: wqyang@aust.edu.cn (W. Yang).

https://doi.org/10.1016/j.ast.2024.109726
Received 3 September 2024; Received in revised form 17 October 2024; Accepted 10 November 2024
Available online 14 November 2024

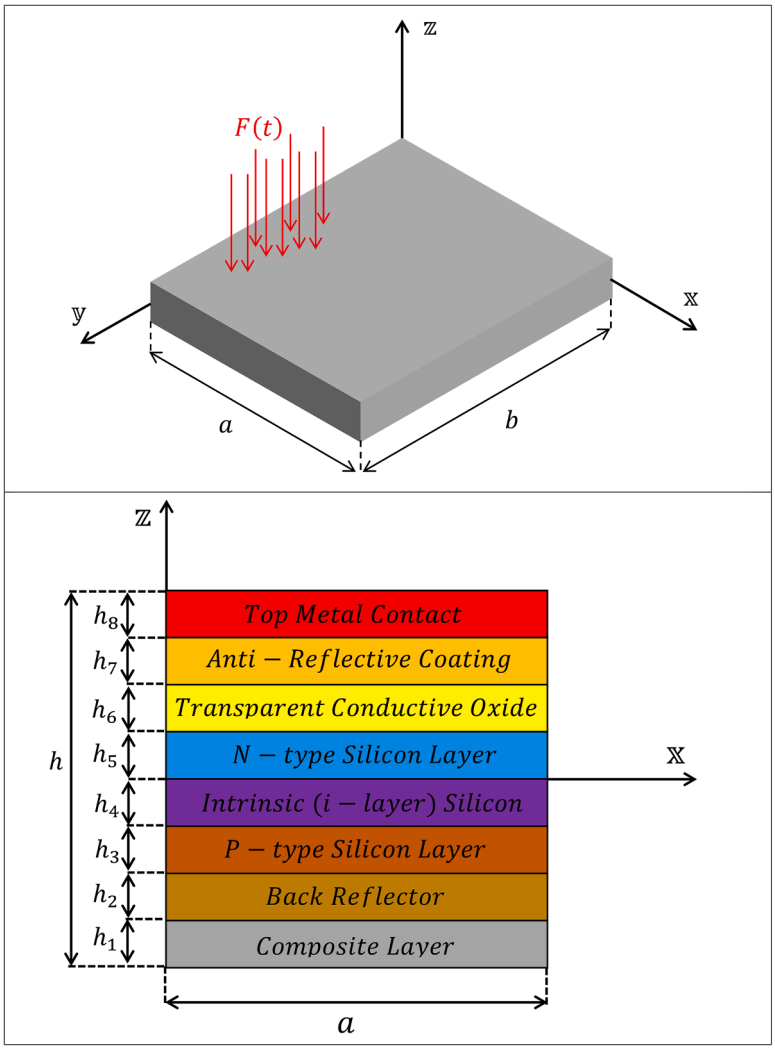

Fig. 1. Multi-layer silicon solar cells under mechanical load.

UV radiation [11]. This resilience makes them suitable for a wide range of applications, from residential rooftop installations to utility-scale solar farms [12]. Additionally, the well-established manufacturing processes of silicon-based cells enable precise control over cell performance and quality, ensuring consistent energy output [13]. Engineers can integrate these cells into diverse energy systems, facilitating their role in smart grids and hybrid energy networks [14]. Furthermore, the modular nature of silicon solar cell arrays allows for easy scalability, enabling flexible design solutions for both small and large energy demands [15]. Finally, ongoing advancements in silicon cell technologies, such as passivated emitter rear cells (PERC), enhance their efficiency, making them even more attractive for engineers looking to optimize energy conversion and system performance [16].

Stability analysis of structures is critical in engineering as it ensures that buildings, bridges, and other infrastructures can withstand applied loads without undergoing failure or collapse [17]. By assessing stability, engineers can prevent structural buckling, which occurs when compressive forces exceed the material's capacity, leading to catastrophic failures [18]. It helps in identifying potential weak points in a structure's design, allowing for reinforcement before construction, thereby improving overall safety [19]. Stability analysis also plays a vital role in optimizing material use, ensuring that structures are designed efficiently without being overly conservative or prone to failure [20]. Moreover, understanding the stability of structures allows engineers to account for external factors like wind, seismic activity, and temperature changes, which can induce additional stress on buildings [21]. This is especially important for high-rise structures, long-span bridges, and large-scale infrastructure projects, where stability concerns are more pronounced due to complex load distributions [22]. Engineers rely on stability analysis to ensure compliance with safety codes and standards, which are essential for protecting lives and property [23]. It also aids in the design of more innovative structures, where unconventional forms and materials are used, ensuring that they remain secure under various load conditions [24]. Stability analysis supports long-term sustainability by minimizing the risk of structural degradation over time, reducing maintenance costs [25]. Finally, it provides a scientific foundation for retrofitting existing structures to improve their resistance to modern load demands and environmental conditions [26].

Machine learning algorithms are crucial for engineers as they enable automation of complex tasks, increasing efficiency and productivity [27, 42]. They help in predictive maintenance, allowing engineers to anticipate equipment failures and reduce downtime [28]. By analyzing vast amounts of data, machine learning can optimize system designs and processes, leading to cost savings and performance improvements [29]. It enhances decision-making by providing data-driven insights and identifying patterns that may not be obvious [30]. Engineers can use machine learning to develop smarter systems, such as self-driving cars or automated manufacturing lines [31]. These algorithms also aid in simulations and modeling, improving accuracy and reducing testing time [32]. Overall, machine learning empowers engineers to innovate and

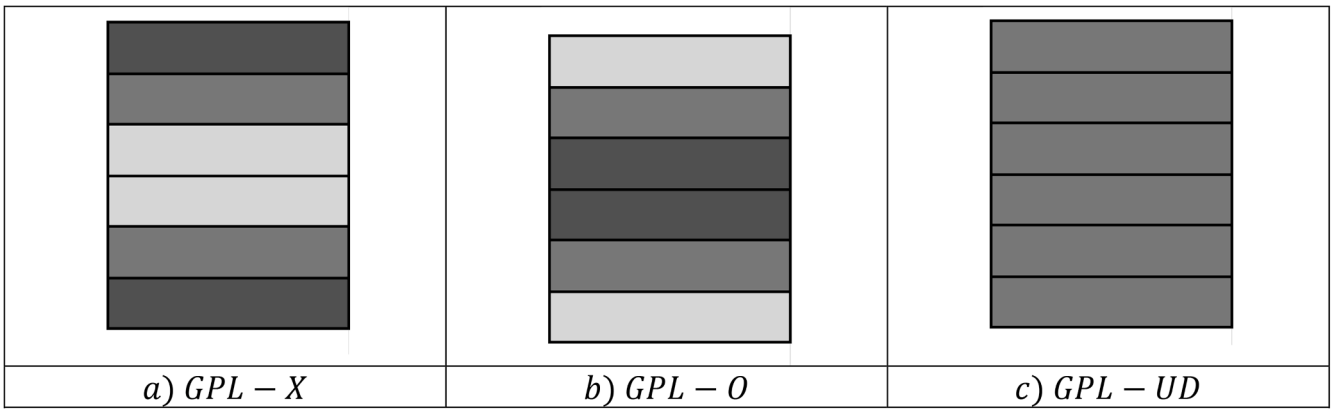

Fig. 2. Various distribution patterns of GPL.

Table 1
The GPLs and metal layer's geometry and material characteristics.

Source	Symbol	Value	Unit
GPL	ν_{GPL}	0.186	–
	ρ_{GPL}	1.06×10^3	kg/m^3
	E_{GPL}	1.01×10^9	Pa
	l_{GPL}	2.5×10^{-6}	m
	w_{GPL}	1.5×10^{-6}	m
	t_{GPL}	1.5×10^{-9}	m
Aluminum epoxy (matrix)	ν_m	0.35	–
	ρ_m	2601	kg/m^3
	E_m	70×10^9	Pa

Table 2
An inventory of the properties of the ingredients that go into making the more advanced, contemporary silicon solar cells [37].

Layey	Material	h	E	ρ	ν
1	**GPLRC**	50 $[\mu m]$	E_c	ρ_c	ν_c
2	**Back Reflector**	350 $[nm]$	69 $[GPa]$	2700	0.33
3	**P-type Silicon Layer**	5 $[\mu m]$	75 $[GPa]$	2330	0.3
4	**Intrinsic (i-layer) Silicon**	250 $[nm]$	75 $[GPa]$	2330	0.3
5	**N-type Silicon Layer**	35 $[nm]$	75 $[GPa]$	2330	0.3
6	**Transparent Conductive Oxide**	200 $[nm]$	120 $[GPa]$	7140	0.25
7	**Anti-Reflective Coating**	70 $[nm]$	200 $[GPa]$	3170	0.28
8	**Top Metal Contact**	150 $[nm]$	83 $[GPa]$	10,490	0.37

solve real-world problems more effectively [33].

The propagation of nonlinear guided waves in enhanced silicon solar cells reinforced by graphene platelet nanocomposites is examined in this work. In order to account for actual shear deformation behavior, the microplate model of the solar cells is built utilizing the modified couple stress theory to capture size-dependent effects and the sinusoidal shear deformation theory. Using Hamilton's principle, nonlinear governing equations defining the system's dynamic response are developed. The phase velocity and wave properties under different parameter values are then analyzed by numerical solution of the equations using the Runge–Kutta technique. We investigate in detail how wavenumber, length scale parameter, and GPL weight percentage affect wave propagation. Using datasets produced from mathematical simulations, this study uses an intelligent model based on deep neural networks as an artificial intelligence algorithm coupled with a genetic algorithm as a bio-inspired optimization approach to predict nonlinear phenomena in guided waves within the solar cell. The findings show that the addition of GPL nanocomposites improves the silicon solar cells' mechanical characteristics, which raises phase velocities and increases wave propagation efficiency. Furthermore, it is discovered that the length scale parameter significantly affects phase velocity, especially at low wavenumbers. This work offers important new information on how to optimize sophisticated silicon solar cells reinforced with nanocomposite materials for uses needing effective guided wave propagation. The results provide a viable strategy for the development and improvement of solar cells in the future.

2. Mathematical modeling

We provide enhanced silicon solar cells using GPL nanocomposites in Fig. 1. A silicon solar cell, as can be seen, is made up of eight layers, with glass at the outermost and the GPLRC-reinforced metal layer at the innermost. Fig. 1 displays the whole geometry of this structure together with a three-dimensional schematic depiction.

2.1. Material properties

As seen in Fig. 2, three different patterns are used to mimic the transverse dispersion of GPLs. To determine the effective elastic modulus of the GPLR nanocomposite material, the following formula was extracted using a modified formulation of the Halpin-Tsai correlation [34]:

$$E_c(\mathbb{z}) = -\frac{3}{8}\frac{1+\xi_L\eta_L V_{GPL}}{\eta_L V_{GPL}-1}\times E_m - \frac{5}{8}\frac{1+\xi_W\eta_W V_{GPL}}{\eta_W V_{GPL}-1}\times E_m, \tag{1}$$

where $\xi_L = 2\frac{L_{GPL}}{t_{GPL}}$, $\xi_W = 2\frac{W_{GPL}}{t_{GPL}}$, $V^*_{GPL} = \frac{W_{GPL}}{\left(\frac{\rho_{GPL}}{\rho_m}\right)(1-W_{GPL})+W_{GPL}}$, $\eta_W = -\frac{1-\left(\frac{E_{GPL}}{E_m}\right)}{\xi_W+\left(\frac{E_{GPL}}{E_m}\right)}$, and $\eta_L = \frac{\left(\frac{E_{GPL}}{E_m}\right)-1}{\left(\frac{E_{GPL}}{E_m}\right)+\xi_L}$. The effective mass density and Poisson's ratio of the composite plate would be obtained as follows using the law of mixtures [35]:

$$\begin{aligned}\rho_c(\mathbb{z}) &= \rho_{GPL}V_{GPL} + \rho_m(1-V_{GPL}),\\ \nu_c(\mathbb{z}) &= \nu_{GPL}V_{GPL} + \nu_m(1-V_{GPL}).\end{aligned} \tag{2}$$

while the effective shear modulus is defined as [36]

$$G_c(\mathbb{z}) = \frac{E_c(\mathbb{z})}{2(1+\nu_c(\mathbb{z}))} \tag{3}$$

We choose three distinct GPL scattering patterns in the structure's thickness direction, as shown in Fig. 2 as well. These patterns' analytical expressions look like this.

$$\begin{aligned}
\text{GPL}-\text{X}: \; V_{GPL} &= 4V^{*}_{GPL}\frac{\left|\mathbb{z}+\frac{h}{2}-\frac{h_1}{2}\right|}{h_1},\\
\text{GPL}-\text{O}: \; V_{GPL} &= 2V^{*}_{GPL}\left(1-2\frac{\left|\mathbb{z}+\frac{h}{2}-\frac{h_1}{2}\right|}{h_1}\right),\\
\text{GPL}-\text{UD}: \; V_{GPL} &= V^{*}_{GPL}.
\end{aligned} \tag{4}$$

Where $\mathbb{z}=\frac{(k-1)h_1}{N_L-1}-\frac{h}{2}$, $k=1,\ldots,N_L$.

Table 1 lists the characteristics of the materials that were used.

Table 2 also provides a summary of the characteristics of the materials used to create the contemporary, enhanced silicon solar cells.

2.2. Kinematic relations

The studied plate at micro size is taken for granted in this work. According to Fig. 1, the lattice plate is h in thickness and a, b, and c in length and breadth, respectively. The mechanical analysis of the enhanced silicon solar cell is done in this work using modified couple stress theory and sinusoidal shear deformation theory. Based on the sinusoidal shear deformation theory (SSDT), the displacement components of the designated enhanced silicon solar cell may be expressed as follows:

$$\begin{aligned}
\mathscr{U}(\mathbb{x},\mathbb{y},\mathbb{z},t) &= \mathscr{U}_0(\mathbb{x},\mathbb{y},t)-\mathbb{z}\frac{\partial w\,\mathscr{W}_0(\mathbb{x},\mathbb{y},t)}{\partial \mathbb{x}}\\
&\quad+\frac{h}{\pi}sin\left(\frac{\pi\mathbb{z}}{h}\right)\left(\frac{\partial \mathscr{W}_0(\mathbb{x},\mathbb{y},t)}{\partial \mathbb{x}}-\Im_{\mathbb{x}}(\mathbb{x},\mathbb{y},t)\right),
\end{aligned} \tag{5a}$$

$$\begin{aligned}
\mathscr{V}(\mathbb{x},\mathbb{y},\mathbb{z},t) &= \mathscr{V}_0(\mathbb{x},\mathbb{y},t)-\mathbb{z}\frac{\partial \mathscr{W}_0(\mathbb{x},\mathbb{y},t)}{\partial \mathbb{y}}\\
&\quad+\frac{h}{\pi}sin\left(\frac{\pi\mathbb{z}}{h}\right)\left(\frac{\partial \mathscr{W}_0(\mathbb{x},\mathbb{y},t)}{\partial \mathbb{y}}-\Im_{\mathbb{y}}(\mathbb{x},\mathbb{y},t)\right),
\end{aligned} \tag{5b}$$

$$\mathscr{W}(\mathbb{x},\mathbb{y},\mathbb{z},t)=\mathscr{W}_0(\mathbb{x},\mathbb{y},t). \tag{5c}$$

where $\Im_{\mathbb{x}}$ and $\Im_{\mathbb{y}}$ are the angles of rotation of the cross sections about the y and x axes of any point on the mid-plane of the microplate, respectively, and $\mathscr{U}$, $\mathscr{V}$, and $\mathscr{W}$ are the $\mathbb{x}$-, $\mathbb{y}$-, and $\mathbb{z}$-components of the displacement vector. Additionally, $\mathscr{U}_0$, $\mathscr{V}_0$ and $\mathscr{W}_0$ are the mid-plane displacements of the microplate in $\mathbb{x}$, $\mathbb{y}$, and $\mathbb{z}$ directions. The strain components are represented as [38] in accordance with the introduced displacement.

$$\mathscr{E}_{\mathbb{x}\mathbb{x}}=\frac{\partial \mathscr{U}(\mathbb{x},\mathbb{y},\mathbb{z},t)}{\partial \mathbb{x}}+\frac{1}{2}\left(\frac{\partial \mathscr{W}(\mathbb{x},\mathbb{y},\mathbb{z},t)}{\partial \mathbb{x}}\right)^2, \tag{6a}$$

$$\mathscr{E}_{\mathbb{y}\mathbb{y}}=\frac{\partial \mathscr{V}(\mathbb{x},\mathbb{y},\mathbb{z},t)}{\partial \mathbb{y}}+\frac{1}{2}\left(\frac{\partial \mathscr{W}(\mathbb{x},\mathbb{y},\mathbb{z},t)}{\partial \mathbb{y}}\right)^2, \tag{6b}$$

$$\begin{aligned}
\mathscr{E}_{\mathbb{x}\mathbb{y}} &= \frac{1}{2}\frac{\partial}{\partial \mathbb{x}}\mathscr{V}(\mathbb{x},\mathbb{y},\mathbb{z},t)+\frac{1}{2}\frac{\partial}{\partial \mathbb{y}}\mathscr{U}(\mathbb{x},\mathbb{y},\mathbb{z},t)\\
&\quad+\frac{1}{2}\frac{\partial \mathscr{W}(\mathbb{x},\mathbb{y},\mathbb{z},t)}{\partial \mathbb{x}}\frac{\partial \mathscr{W}(\mathbb{x},\mathbb{y},\mathbb{z},t)}{\partial \mathbb{y}},
\end{aligned} \tag{6c}$$

$$\mathscr{E}_{\mathbb{x}\mathbb{z}}=\frac{1}{2}\left(\frac{\partial \mathscr{W}(\mathbb{x},\mathbb{y},\mathbb{z},t)}{\partial \mathbb{x}}+\frac{\partial \mathscr{U}(\mathbb{x},\mathbb{y},\mathbb{z},t)}{\partial \mathbb{z}}\right), \tag{6d}$$

$$\mathscr{E}_{\mathbb{y}\mathbb{z}}=\frac{1}{2}\left(\frac{\partial \mathscr{W}(\mathbb{x},\mathbb{y},\mathbb{z},t)}{\partial \mathbb{y}}+\frac{\partial \mathscr{V}(\mathbb{x},\mathbb{y},\mathbb{z},t)}{\partial \mathbb{z}}\right). \tag{6e}$$

The constitutive relations [38] of the silicon solar cell is

$$\begin{Bmatrix}\mathscr{T}_{\mathbb{x}\mathbb{x}}\\ \mathscr{T}_{\mathbb{y}\mathbb{y}}\\ \mathscr{T}_{\mathbb{y}\mathbb{z}}\\ \mathscr{T}_{\mathbb{x}\mathbb{z}}\\ \mathscr{T}_{\mathbb{x}\mathbb{y}}\end{Bmatrix}=\begin{Bmatrix}\mathscr{Y}_{11} & \mathscr{Y}_{12} & 0 & 0 & 0\\ \mathscr{Y}_{21} & \mathscr{Y}_{22} & 0 & 0 & 0\\ 0 & 0 & \mathscr{Y}_{44} & 0 & 0\\ 0 & 0 & 0 & \mathscr{Y}_{55} & 0\\ 0 & 0 & 0 & 0 & \mathscr{Y}_{66}\end{Bmatrix}\begin{Bmatrix}\mathscr{E}_{\mathbb{x}\mathbb{x}}\\ \mathscr{E}_{\mathbb{y}\mathbb{y}}\\ 2\mathscr{E}_{\mathbb{y}\mathbb{z}}\\ 2\mathscr{E}_{\mathbb{x}\mathbb{z}}\\ 2\mathscr{E}_{\mathbb{x}\mathbb{y}}\end{Bmatrix}. \tag{7}$$

```
% Genetic Algorithm for Optimizing a Neural Network (DNN-GA)
% Predicting Nonlinear Wave Propagation in Silicon Solar Cells
% Initialization
% Example data (replace this with actual training data)
% X_train: input features for training
% y_train: output labels for training (target values)
% Neural Network Parameters
% Initialize GA Population (Random Weights and Biases)
% Chromosome: Flattened vector of weights and biases
% Fitness Function: Mean Squared Error (MSE)
% Start the GA optimization process
      % Evaluate fitness for each individual in the population
         % Select parents based on fitness (best individuals)
         % Generate offspring through crossover
         % Apply mutation to the offspring
   % Create new population: Combine parents and offspring
% Final optimized weights and biases
% Neural Network Prediction using the optimized individual
% --- Supporting Functions ---
% Mean Squared Error function
% Neural Network Forward Pass (Single Layer)
   % Unpack weights and biases from the chromosome
      % Input-to-Hidden Layer Weights and Biases
      % Hidden-to-Output Layer Weights and Biases
        % Forward Pass (Activation: ReLU for hidden layer, Linear for output layer)
   % Crossover Function
% Mutation Function
```

Fig. 3. A MATLAB implementation of the hybrid algorithm combining a deep neural network with a genetic algorithm for predicting nonlinear wave propagation.

where $\mathscr{T}_{xx}$ and $\mathscr{T}_{yy}$ are the normal stress factor, $\mathscr{T}_{yz}$, $\mathscr{T}_{xz}$ and $\mathscr{T}_{xy}$ are the shear stress factor, $\mathscr{Y}_{ij}$ is the stiffness coefficient of the silicon solar cell, and there are

$$\mathscr{Y}_{11}=\frac{E_i}{1-\nu_i^2},\ \mathscr{Y}_{12}=\mathscr{Y}_{21}=\frac{\nu_i E_i}{1-\nu_i^2},\ \mathscr{Y}_{22}=\frac{E_i}{1-\nu_i^2}, \tag{8a}$$

$$\mathscr{Y}_{66}=\frac{E_i}{2(1+\nu_i)},\ \mathscr{Y}_{44}=\frac{E_i}{2(1+\nu_i)},\ \mathscr{Y}_{55}=\frac{E_i}{2(1+\nu_i)},\ i=1,\ldots,8. \tag{8b}$$

3. Modified couple stress formulation

The additional term is added to the classical strain energy to introduce the modified pair stress theory. According to the modified couple stress theory, the plate's strain energy is defined as follows [39]:

$$U=\int_V\{(\mathscr{T}_{xx}\mathscr{E}_{xx}+\mathscr{T}_{yy}\mathscr{E}_{yy}+2\mathscr{T}_{xz}\mathscr{E}_{xz}+2\mathscr{T}_{xy}\mathscr{E}_{xy}+2\mathscr{T}_{yz}\mathscr{E}_{yz}) + (\mathbb{m}_{xx}\chi_{xx}+\mathbb{m}_{yy}\chi_{yy}+\mathbb{m}_{zz}\chi_{zz}+2\mathbb{m}_{xy}\chi_{xy}+2\mathbb{m}_{yz}\chi_{yz}+2\mathbb{m}_{xz}\chi_{xz})\}dV, \tag{9}$$

In which:

$$\chi_{ij}=\frac{1}{2}(\theta_{i,j}+\theta_{j,i}), \tag{10a}$$

$$\theta_i=\frac{1}{2}e_{ijk}\mathscr{U}_{k,j}. \tag{10b}$$

where e_{ijk} is permutation symbol. Also, the non-classical term of stress $(\mathbb{m}_{ij})$ is presented as [20]:

$$\mathbb{m}_{ij}=2\mu l^2\chi_{ij}, \tag{11}$$

where μ is the shear modulus and l is the extra material length scale parameters important to rotation gradient. As a result:

$$\mu=\frac{E_i}{2(1+\nu_i)}, \tag{12}$$

The set of governing equations of motion is given by Eq. (9), which also involves carrying out mathematical operations and the initial variation of the kinetic energy and the variation of the strain energy. Where A is area of the plate. By operating $d\mathbb{z}$ on $\mathscr{T}_{ij}$ and $\mathbb{m}_{ij}$ the resultant components are defined as:

$$\int_{-\frac{h}{2}}^{\frac{h}{2}}d\mathbb{z}=\int_{-\frac{h}{2}}^{-\frac{h}{2}+h_1}d\mathbb{z}+\int_{-\frac{h}{2}+h_1}^{-\frac{h}{2}+h_1+h_2}d\mathbb{z}+\int_{-h_3-h_4}^{-h_4}d\mathbb{z}+\int_{-h_4}^{0}d\mathbb{z}+\int_{0}^{h_5}d\mathbb{z}+\int_{h_5}^{h_5+h_6}d\mathbb{z} + \int_{h_5+h_6}^{h_5+h_6+h_7}d\mathbb{z}+\int_{\frac{h}{2}-h_8}^{\frac{h}{2}}d\mathbb{z}. \tag{13a}$$

$$\left\{\mathfrak{N}_{ij},\mathfrak{M}_{ij},\mathfrak{P}_{ij},\mathfrak{P}^*_{ij},\mathfrak{Q}_{ij}\right\}=\int_{-\frac{h}{2}}^{\frac{h}{2}}\left(1,\mathbb{z},\frac{h}{\pi}sin\left(\frac{\pi\mathbb{z}}{h}\right),\frac{\pi}{h}\sin\left(\frac{\pi\mathbb{z}}{h}\right),\cos\left(\frac{\pi\mathbb{z}}{h}\right)\right)\mathscr{T}_{ij}d\mathbb{z}, \tag{13b}$$

Table 3
Comparison of present results for the circular frequencies (ω) with the results of Ref. [41] for various wave number.

	$K_x=K_y$				
	2	5	8	11	14
Present	128.24	800.81	2047.45	3862.81	6239.88
Ref. [41]	128.26	800.97	2047.55	3863.09	6240.55

$$\left\{\mathfrak{H}_{ij},\mathfrak{K}_{ij},\mathfrak{K}^*_{ij},\mathfrak{L}_{ij}\right\}=\int_{-\frac{h}{2}}^{\frac{h}{2}}\left(1,\frac{h}{\pi}\sin\left(\frac{\pi\mathbb{z}}{h}\right),\frac{\pi}{h}\sin\left(\frac{\pi\mathbb{z}}{h}\right),\cos\left(\frac{\pi\mathbb{z}}{h}\right)\right)\mathbb{m}_{ij}d\mathbb{z}. \tag{13c}$$

When the consequent components from Eqs. (13b-c) are substituted, the strain energy takes on the following final variation form:

$$\begin{aligned}\delta U &= \delta U_1+\delta U_2=\int\int\Big\{\Big(\Big(-\frac{\partial\mathfrak{N}_{xx}}{\partial\mathbb{x}}-\frac{\partial\mathfrak{N}_{xy}}{\partial\mathbb{y}}\Big)\delta\mathscr{U}+\Big(-\frac{\partial\mathfrak{N}_{xy}}{\partial\mathbb{x}}-\frac{\partial\mathfrak{N}_{yy}}{\partial\mathbb{y}}\Big)\delta\mathscr{V}+\Big(-\frac{\partial^2\mathfrak{M}_{xx}}{\partial\mathbb{x}^2}+\frac{\partial^2\mathfrak{P}_{xx}}{\partial\mathbb{x}^2}-2\frac{\partial^2\mathfrak{M}_{xy}}{\partial\mathbb{y}\partial\mathbb{x}}+2\frac{\partial^2\mathfrak{P}_{xy}}{\partial\mathbb{y}\partial\mathbb{x}}-\frac{\partial\mathfrak{Q}_{xz}}{\partial\mathbb{x}}\\
&-\frac{\partial^2\mathfrak{M}_{yy}}{\partial\mathbb{y}^2}+\frac{\partial^2\mathfrak{P}_{yy}}{\partial\mathbb{y}^2}-\frac{\partial\mathfrak{Q}_{yz}}{\partial\mathbb{y}}+\frac{\partial}{\partial\mathbb{x}}\Big(\mathfrak{N}_{xx}\frac{\partial\mathscr{W}}{\partial\mathbb{x}}\Big)+\frac{\partial}{\partial\mathbb{y}}\Big(\mathfrak{N}_{yy}\frac{\partial\mathscr{W}}{\partial\mathbb{y}}\Big)\\
&+\frac{\partial}{\partial\mathbb{y}}\Big(\mathfrak{N}_{xy}\frac{\partial\mathscr{W}}{\partial\mathbb{x}}\Big)+\frac{\partial}{\partial\mathbb{x}}\Big(\mathfrak{N}_{xy}\frac{\partial\mathscr{W}}{\partial\mathbb{y}}\Big)\Big)\delta\mathscr{W}+\Big(\frac{\partial\mathfrak{P}_{xx}}{\partial\mathbb{x}}+\frac{\partial\mathfrak{P}_{xy}}{\partial\mathbb{y}}-\mathfrak{Q}_{xz}\Big)\delta\widetilde{\mathfrak{F}}_x\\
&+\Big(\frac{\partial\mathfrak{P}_{xy}}{\partial\mathbb{x}}+\frac{\partial\mathfrak{P}_{yy}}{\partial\mathbb{y}}-\mathfrak{Q}_{yz}\Big)\delta\widetilde{\mathfrak{F}}_y\Big)+\Big(\Big(-\frac{\partial^2\mathfrak{H}_{yz}}{2\partial\mathbb{y}^2}-\frac{\partial^2\mathfrak{H}_{xz}}{2\partial\mathbb{y}\partial\mathbb{x}}\Big)\delta\mathscr{U}+\Big(\frac{\partial^2\mathfrak{H}_{yz}}{2\partial\mathbb{y}\partial\mathbb{x}}\\
&+\frac{\partial^2\mathfrak{H}_{xz}}{2\partial\mathbb{x}^2}\Big)\delta\mathscr{V}+\Big(-\frac{1}{2}\frac{\partial\mathfrak{K}^*_{xz}}{\partial\mathbb{y}}+\frac{1}{2}\frac{\partial\mathfrak{K}^*_{yz}}{\partial\mathbb{x}}-\frac{\partial^2\mathfrak{H}_{yy}}{\partial\mathbb{y}\partial\mathbb{x}}+\frac{\partial^2\mathfrak{H}_{xy}}{\partial\mathbb{y}^2}+\frac{\partial^2\mathfrak{H}_{xx}}{\partial\mathbb{y}\partial\mathbb{x}}\\
&-\frac{\partial^2\mathfrak{H}_{xy}}{\partial\mathbb{x}^2}+\frac{\partial^2\mathfrak{L}_{yy}}{2\partial\mathbb{y}\partial\mathbb{x}}-\frac{\partial^2\mathfrak{L}_{xy}}{2\partial\mathbb{y}^2}+\frac{\partial^2\mathfrak{L}_{xy}}{2\partial\mathbb{x}^2}-\frac{\partial^2\mathfrak{L}_{xx}}{2\partial\mathbb{y}\partial\mathbb{x}}\Big)\delta\mathscr{W}+\Big(\frac{1}{2}\frac{\partial^2\mathfrak{K}_{xz}}{\partial\mathbb{y}\partial\mathbb{x}}+\frac{\partial\mathfrak{Q}_{yy}}{2\partial\mathbb{y}}\\
&+\frac{\partial\mathfrak{Q}_{xy}}{2\partial\mathbb{x}}-\frac{\partial\mathfrak{Q}_{zz}}{2\partial\mathbb{y}}+\frac{\mathfrak{K}^*_{yz}}{2}+\frac{1}{2}\frac{\partial^2\mathfrak{K}_{yz}}{\partial\mathbb{y}^2}\Big)\delta\widetilde{\mathfrak{F}}_x+\Big(-\frac{1}{2}\frac{\partial^2\mathfrak{K}_{xz}}{\partial\mathbb{x}^2}-\frac{\mathfrak{K}^*_{xz}}{2}-\frac{1}{2}\frac{\partial^2\mathfrak{K}_{yz}}{\partial\mathbb{y}\partial\mathbb{x}}\\
&-\frac{\partial\mathfrak{Q}_{xx}}{2\partial\mathbb{x}}-\frac{\partial\mathfrak{Q}_{xy}}{2\partial\mathbb{y}}+\frac{\partial\mathfrak{Q}_{zz}}{2\partial\mathbb{x}}\Big)\delta\widetilde{\mathfrak{F}}_y\Big)\Big\}dA,\end{aligned} \tag{14}$$

where U_1 denotes the strain energy's classical component and U_2 denotes its non-classical component. The kinetic energy fluctuation is written as:

$$\begin{aligned}\delta T=\int\int\Big\{&\Big(-\mathscr{I}_0\frac{\partial^2\mathscr{U}}{\partial t^2}+\mathscr{I}_1\frac{\partial^3\mathscr{W}}{\partial\mathbb{x}\partial t^2}-\mathscr{I}_3\frac{\partial^3\mathscr{W}}{\partial\mathbb{x}\partial t^2}+\mathscr{I}_3\frac{\partial^2\widetilde{\mathfrak{F}}_x}{\partial t^2}\Big)\delta\mathscr{U}+\Big(-\mathscr{I}_0\frac{\partial^2\mathscr{V}}{\partial t^2}+\mathscr{I}_1\frac{\partial^3\mathscr{W}}{\partial\mathbb{y}\partial t^2}-\mathscr{I}_3\frac{\partial^3\mathscr{W}}{\partial\mathbb{y}\partial t^2}+\mathscr{I}_3\frac{\partial^2\widetilde{\mathfrak{F}}_y}{\partial t^2}\Big)\delta\mathscr{V}\\
&+\Big(-\mathscr{I}_1\frac{\partial^3\mathscr{U}}{\partial\mathbb{x}\partial t^2}+\mathscr{I}_3\frac{\partial^3\mathscr{U}}{\partial\mathbb{x}\partial t^2}+\mathscr{I}_2\frac{\partial^4\mathscr{W}}{\partial\mathbb{x}^2\partial t^2}-2\mathscr{I}_5\frac{\partial^4\mathscr{W}}{\partial\mathbb{x}^2\partial t^2}+\mathscr{I}_5\frac{\partial^3\widetilde{\mathfrak{F}}_x}{\partial\mathbb{x}\partial t^2}\\
&+\mathscr{I}_4\frac{\partial^4\mathscr{W}}{\partial\mathbb{x}^2\partial t^2}-\mathscr{I}_4\frac{\partial^3\widetilde{\mathfrak{F}}_x}{\partial\mathbb{x}\partial t^2}-\mathscr{I}_1\frac{\partial^3\mathscr{V}}{\partial\mathbb{y}\partial t^2}+\mathscr{I}_3\frac{\partial^3\mathscr{V}}{\partial\mathbb{y}\partial t^2}+\mathscr{I}_2\frac{\partial^4\mathscr{W}}{\partial\mathbb{y}^2\partial t^2}\\
&-2\mathscr{I}_5\frac{\partial^4\mathscr{W}}{\partial\mathbb{y}^2\partial t^2}+\mathscr{I}_5\frac{\partial^3\widetilde{\mathfrak{F}}_y}{\partial\mathbb{y}\partial t^2}+\mathscr{I}_4\frac{\partial^4\mathscr{W}}{\partial\mathbb{y}^2\partial t^2}-\mathscr{I}_4\frac{\partial^3\widetilde{\mathfrak{F}}_y}{\partial\mathbb{y}\partial t^2}-\mathscr{I}_0\frac{\partial^2\mathscr{W}}{\partial t^2})\\
&\delta\mathscr{W}+\Big(\mathscr{I}_3\frac{\partial^2\mathscr{U}}{\partial t^2}-\mathscr{I}_5\frac{\partial^3\mathscr{W}}{\partial\mathbb{x}\partial t^2}+\mathscr{I}_4\frac{\partial^3\mathscr{W}}{\partial\mathbb{x}\partial t^2}-\mathscr{I}_4\frac{\partial^2\widetilde{\mathfrak{F}}_x}{\partial t^2}\Big)\delta\widetilde{\mathfrak{F}}_x\\
&+\Big(\mathscr{I}_3\frac{\partial^2\mathscr{V}}{\partial t^2}-\mathscr{I}_5\frac{\partial^3\mathscr{W}}{\partial\mathbb{y}\partial t^2}+\mathscr{I}_4\frac{\partial^3\mathscr{W}}{\partial\mathbb{y}\partial t^2}-\mathscr{I}_4\frac{\partial^2\widetilde{\mathfrak{F}}_y}{\partial t^2}\Big)\delta\widetilde{\mathfrak{F}}_y\Big\}dA,\end{aligned} \tag{15}$$

where the integration constants are defined as:

$$\int_{-\frac{h}{2}}^{\frac{h}{2}}d\mathbb{z}=\int_{-\frac{h}{2}}^{-\frac{h}{2}+h_1}d\mathbb{z}+\int_{-\frac{h}{2}+h_1}^{-\frac{h}{2}+h_1+h_2}d\mathbb{z}+\int_{-h_3-h_4}^{-h_4}d\mathbb{z}+\int_{-h_4}^{0}d\mathbb{z}+\int_{0}^{h_5}d\mathbb{z}+\int_{h_5}^{h_5+h_6}d\mathbb{z} + \int_{h_5+h_6}^{h_5+h_6+h_7}d\mathbb{z}+\int_{\frac{h}{2}-h_8}^{\frac{h}{2}}d\mathbb{z}. \tag{16a}$$

$$\{\mathscr{I}_0,\mathscr{I}_1,\mathscr{I}_2,\mathscr{I}_3,\mathscr{I}_4,\mathscr{I}_5\}=\int_{-\frac{h}{2}}^{\frac{h}{2}}\rho\left\{1,\mathbb{z},\mathbb{z}^2,\frac{h}{\pi}\sin\left(\frac{\pi\mathbb{z}}{h}\right),\frac{h^2}{\pi^2}\sin2\left(\frac{\pi\mathbb{z}}{h}\right),\frac{h\mathbb{z}}{\pi}\sin\left(\frac{\pi\mathbb{z}}{h}\right)\right\}d\mathbb{z}, \tag{16b}$$

Also, the virtual work done by external forces δW of the system can be expressed respectively as

$$\delta W=\iint F\delta\mathscr{W}dA. \tag{17}$$

In which, $F=Psin(\Omega_{ext}t)$ where P is the load intensity and Ω_{ext} denotes the excitation frequency.

According to the Hamilton's principle, five equations of motion that govern the problem are obtained as:

$$\begin{aligned}&-\mathscr{I}_0\frac{\partial^2\mathscr{U}}{\partial t^2}+\mathscr{I}_1\frac{\partial^3\mathscr{W}}{\partial\mathbb{x}\partial t^2}-\mathscr{I}_3\frac{\partial^3\mathscr{W}}{\partial\mathbb{x}\partial t^2}+\mathscr{I}_3\frac{\partial^2\widetilde{\mathfrak{F}}_{\mathbb{y}}}{\partial t^2}+\frac{\partial^2\mathfrak{S}_{\mathbb{yz}}}{2\partial\mathbb{y}^2}+\frac{\partial^2\mathfrak{S}_{\mathbb{xz}}}{2\partial\mathbb{y}\partial\mathbb{x}}+\frac{\partial\mathfrak{N}_{\mathbb{xx}}}{\partial\mathbb{x}}\\&+\frac{\partial\mathfrak{N}_{\mathbb{xy}}}{\partial\mathbb{y}}\\&=0,\end{aligned} \tag{18a}$$

$$\begin{aligned}&\mathscr{I}_3\frac{\partial^2\widetilde{\mathfrak{F}}_{\mathbb{y}}}{\partial t^2}+\mathscr{I}_1\frac{\partial^3\mathscr{W}}{\partial\mathbb{y}\partial t^2}-\mathscr{I}_0\frac{\partial^2\mathscr{V}}{\partial t^2}-\mathscr{I}_3\frac{\partial^3\mathscr{W}}{\partial\mathbb{y}\partial t^2}-\frac{\partial^2\mathfrak{S}_{\mathbb{yz}}}{2\partial\mathbb{y}\partial\mathbb{x}}-\frac{\partial^2\mathfrak{S}_{\mathbb{xz}}}{2\partial\mathbb{x}^2}+\frac{\partial\mathfrak{N}_{\mathbb{xy}}}{\partial\mathbb{x}}\\&+\frac{\partial\mathfrak{N}_{\mathbb{yy}}}{\partial\mathbb{y}}\\&=0,\end{aligned} \tag{18b}$$

$$\begin{aligned}&\mathscr{I}_3\frac{\partial^3\mathscr{U}}{\partial\mathbb{x}\partial t^2}-\mathscr{I}_1\frac{\partial^3\mathscr{U}}{\partial\mathbb{x}\partial t^2}+\mathscr{I}_3\frac{\partial^3\mathscr{V}}{\partial\mathbb{y}\partial t^2}-\mathscr{I}_1\frac{\partial^3\mathscr{V}}{\partial\mathbb{y}\partial t^2}-2\mathscr{I}_5\frac{\partial^4\mathscr{W}}{\partial\mathbb{x}^2\partial t^2}-\mathscr{I}_0\frac{\partial^2\mathscr{W}}{\partial t^2}\\&+\mathscr{I}_4\frac{\partial^4\mathscr{W}}{\partial\mathbb{y}^2\partial t^2}+\mathscr{I}_2\frac{\partial^4\mathscr{W}}{\partial\mathbb{y}^2\partial t^2}-2\mathscr{I}_5\frac{\partial^4\mathscr{W}}{\partial\mathbb{y}^2\partial t^2}+\mathscr{I}_2\frac{\partial^4\mathscr{W}}{\partial\mathbb{x}^2\partial t^2}+\mathscr{I}_4\frac{\partial^4\mathscr{W}}{\partial\mathbb{x}^2\partial t^2}-\frac{\partial^2\mathfrak{W}_{\mathbb{xx}}}{\partial\mathbb{x}^2}\\&-\frac{2\partial^2\mathfrak{W}_{\mathbb{xy}}}{\partial\mathbb{y}\partial\mathbb{x}}-\frac{\partial^2\mathfrak{W}_{\mathbb{yy}}}{\partial\mathbb{y}^2}+\mathscr{I}_5\frac{\partial^3\widetilde{\mathfrak{F}}_{\mathbb{y}}}{\partial\mathbb{y}\partial t^2}\end{aligned}$$

$$\begin{aligned}&-\mathscr{I}_4\frac{\partial^3\widetilde{\mathfrak{F}}_{\mathbb{y}}}{\partial\mathbb{y}\partial t^2}-\mathscr{I}_4\frac{\partial^3\widetilde{\mathfrak{F}}_{\mathbb{x}}}{\partial\mathbb{x}\partial t^2}+\mathscr{I}_5\frac{\partial^3\widetilde{\mathfrak{F}}_{\mathbb{x}}}{\partial\mathbb{x}\partial t^2}+\frac{\partial}{\partial\mathbb{x}}\left(\mathfrak{N}_{\mathbb{xx}}\frac{\partial\mathscr{W}}{\partial\mathbb{x}}\right)+\frac{\partial}{\partial\mathbb{y}}\left(\mathfrak{N}_{\mathbb{yy}}\frac{\partial\mathscr{W}}{\partial\mathbb{y}}\right)\\&+\frac{\partial}{\partial\mathbb{y}}\left(\mathfrak{N}_{\mathbb{xy}}\frac{\partial\mathscr{W}}{\partial\mathbb{x}}\right)+\frac{\partial}{\partial\mathbb{x}}\left(\mathfrak{N}_{\mathbb{xy}}\frac{\partial\mathscr{W}}{\partial\mathbb{y}}\right)+\frac{\partial^2\mathfrak{M}_{\mathbb{yy}}}{\partial\mathbb{y}^2}+\frac{2\partial^2\mathfrak{M}_{\mathbb{xy}}}{\partial\mathbb{y}\partial\mathbb{x}}+\frac{\partial^2\mathfrak{M}_{\mathbb{xx}}}{\partial\mathbb{x}^2}+\frac{\partial\mathfrak{Q}_{\mathbb{yz}}}{\partial\mathbb{y}}\end{aligned}$$

$$\begin{aligned}&+\frac{\partial\mathfrak{Q}_{\mathbb{xz}}}{\partial\mathbb{x}}+\frac{\partial\mathfrak{R}^*_{\mathbb{xz}}}{2\partial\mathbb{y}}-\frac{\partial\mathfrak{R}^*_{\mathbb{yz}}}{2\partial\mathbb{x}}-\frac{\partial^2\mathfrak{L}_{\mathbb{yy}}}{2\partial\mathbb{y}\partial\mathbb{x}}-\frac{\partial^2\mathfrak{L}_{\mathbb{xy}}}{2\partial\mathbb{x}^2}+\frac{\partial^2\mathfrak{L}_{\mathbb{xx}}}{2\partial\mathbb{y}\partial\mathbb{x}}+\frac{\partial^2\mathfrak{L}_{\mathbb{xy}}}{2\partial\mathbb{y}^2}-\frac{\partial^2\mathfrak{H}_{\mathbb{xx}}}{\partial\mathbb{y}\partial\mathbb{x}}\\&+\frac{\partial^2\mathfrak{H}_{\mathbb{xy}}}{\partial\mathbb{x}^2}+\frac{\partial^2\mathfrak{H}_{\mathbb{yy}}}{\partial\mathbb{y}\partial\mathbb{x}}-\frac{\partial^2\mathfrak{H}_{\mathbb{xy}}}{\partial\mathbb{y}^2}+F\\&=0,\end{aligned} \tag{18c}$$

$$\begin{aligned}&\mathscr{I}_3\frac{\partial^2\mathscr{U}}{\partial t^2}-\mathscr{I}_5\frac{\partial^3\mathscr{W}}{\partial\mathbb{x}\partial t^2}-\mathscr{I}_4\frac{\partial^2\widetilde{\mathfrak{F}}_{\mathbb{x}}}{\partial t^2}+\mathscr{I}_4\frac{\partial^3\mathscr{W}}{\partial\mathbb{x}\partial t^2}-\frac{\partial^2\mathfrak{R}_{\mathbb{yz}}}{2\partial\mathbb{y}^2}-\frac{\partial^2\mathfrak{R}_{\mathbb{xz}}}{2\partial\mathbb{y}\partial\mathbb{x}}-\frac{\mathfrak{R}^*_{\mathbb{yz}}}{2}-\frac{\partial\mathfrak{Q}_{\mathbb{xy}}}{2\partial\mathbb{x}}\\&+\frac{\partial\mathfrak{Q}_{\mathbb{zz}}}{2\partial\mathbb{y}}-\frac{\partial\mathfrak{Q}_{\mathbb{yy}}}{2\partial\mathbb{y}}-\frac{\partial\mathfrak{W}_{\mathbb{xx}}}{\partial\mathbb{x}}-\frac{\partial\mathfrak{W}_{\mathbb{xy}}}{\partial\mathbb{y}}+\mathfrak{Q}_{\mathbb{xz}}\\&=0,\end{aligned} \tag{18d}$$

$$\begin{aligned}&-\mathscr{I}_4\frac{\partial^2\widetilde{\mathfrak{F}}_{\mathbb{y}}}{\partial t^2}+\mathscr{I}_3\frac{\partial^2\mathscr{V}}{\partial t^2}+\mathscr{I}_4\frac{\partial^3\mathscr{W}}{\partial\mathbb{y}\partial t^2}-\mathscr{I}_5\frac{\partial^3\mathscr{W}}{\partial\mathbb{y}\partial t^2}+\frac{\partial^2\mathfrak{R}_{\mathbb{xz}}}{2\partial\mathbb{x}^2}+\frac{\partial^2\mathfrak{R}_{\mathbb{yz}}}{2\partial\mathbb{y}\partial\mathbb{x}}+\frac{\mathfrak{R}^*_{\mathbb{xz}}}{2}\\&+\frac{\partial\mathfrak{Q}_{\mathbb{xy}}}{2\partial\mathbb{y}}-\frac{\partial\mathfrak{Q}_{\mathbb{zz}}}{2\partial\mathbb{x}}+\frac{\partial\mathfrak{Q}_{\mathbb{xx}}}{2\partial\mathbb{x}}-\frac{\partial\mathfrak{W}_{\mathbb{xy}}}{\partial\mathbb{x}}-\frac{\partial\mathfrak{W}_{\mathbb{yy}}}{\partial\mathbb{y}}+\mathfrak{Q}_{\mathbb{yz}}\\&=0,\end{aligned} \tag{18e}$$

4. Solution method

4.1. Forced nonlinear wave propagation responses

In this section, the Runge–Kutta technique is used to solve the nonlinear forced wave propagation characteristics of the silicon solar sell. Additionally, the following formulae characterize the displacement components:

$$\begin{aligned}\mathscr{U}_0&=\overline{\mathscr{U}}_0(t)e^{i\left(K_x\mathbb{x}+K_y\mathbb{y}\right)},\\\mathscr{V}_0&=\overline{\mathscr{V}}_0(t)e^{i\left(K_x\mathbb{x}+K_y\mathbb{y}\right)},\\\mathscr{W}_0&=\overline{\mathscr{W}}_0(t)e^{i\left(K_x\mathbb{x}+K_y\mathbb{y}\right)},\\\widetilde{\mathfrak{F}}_{\mathbb{x}}&=\overline{\widetilde{\mathfrak{F}}}_{\mathbb{x}}(t)e^{i\left(K_x\mathbb{x}+K_y\mathbb{y}\right)},\\\widetilde{\mathfrak{F}}_{\mathbb{y}}&=\overline{\widetilde{\mathfrak{F}}}_{\mathbb{y}}(t)e^{i\left(K_x\mathbb{x}+K_y\mathbb{y}\right)}.\end{aligned} \tag{19}$$

in which $\overline{\mathscr{U}}_0(t)$, $\overline{\mathscr{V}}_0(t)$, $\overline{\mathscr{W}}_0(t)$, $\overline{\widetilde{\mathfrak{F}}}_{\mathbb{x}}(t)$ and $\overline{\widetilde{\mathfrak{F}}}_{\mathbb{y}}(t)$ stand for five undetermined functions of time. Also, $i=\sqrt{-1}$, K_x, and K_y indicates wave number in $\mathbb{x}$-, and $\mathbb{y}$- directions. By substituting Eqs. (13b), (13c), (16b), and (19), into Eqs. (18a-e), a system of ordinary differential equations can be derived.

$$\begin{aligned}&\mathbb{k}_{11}\overline{\mathscr{U}}_0(t)+\mathbb{k}_{12}\overline{\mathscr{V}}_0(t)+\mathbb{k}_{13}\overline{\mathscr{W}}_0(t)+\mathbb{k}_{14}\overline{\mathscr{W}}_0^2(t)+\mathbb{k}_{15}\overline{\widetilde{\mathfrak{F}}}_{\mathbb{x}}(t)+\mathbb{k}_{16}\overline{\widetilde{\mathfrak{F}}}_{\mathbb{y}}(t)\\&=\mathbb{m}_{11}\ddot{\overline{\mathscr{U}}}_0(t)+\mathbb{m}_{12}\ddot{\overline{\mathscr{V}}}_0(t)+\mathbb{m}_{13}\ddot{\overline{\mathscr{W}}}_0(t)+\mathbb{m}_{14}\ddot{\overline{\widetilde{\mathfrak{F}}}}_{\mathbb{x}}(t)+\mathbb{m}_{15}\ddot{\overline{\widetilde{\mathfrak{F}}}}_{\mathbb{y}}(t),\end{aligned} \tag{20a}$$

$$\begin{aligned}&\mathbb{k}_{21}\overline{\mathscr{U}}_0(t)+\mathbb{k}_{22}\overline{\mathscr{V}}_0(t)+\mathbb{k}_{23}\overline{\mathscr{W}}_0(t)+\mathbb{k}_{24}\overline{\mathscr{W}}_0^2(t)+\mathbb{k}_{25}\overline{\widetilde{\mathfrak{F}}}_{\mathbb{x}}(t)+\mathbb{k}_{26}\overline{\widetilde{\mathfrak{F}}}_{\mathbb{y}}(t)\\&=\mathbb{m}_{21}\ddot{\overline{\mathscr{U}}}_0(t)+\mathbb{m}_{22}\ddot{\overline{\mathscr{V}}}_0(t)+\mathbb{m}_{23}\ddot{\overline{\mathscr{W}}}_0(t)+\mathbb{m}_{24}\ddot{\overline{\widetilde{\mathfrak{F}}}}_{\mathbb{x}}(t)+\mathbb{m}_{25}\ddot{\overline{\widetilde{\mathfrak{F}}}}_{\mathbb{y}}(t),\end{aligned} \tag{20b}$$

$$\begin{aligned}&\mathbb{k}_{31}\overline{\mathscr{U}}_0(t)+\mathbb{k}_{32}\overline{\mathscr{V}}_0(t)+\mathbb{k}_{33}\overline{\mathscr{W}}_0(t)+\mathbb{k}_{34}\overline{\mathscr{W}}_0^2(t)+\mathbb{k}_{35}\overline{\mathscr{W}}_0^3(t)+\mathbb{k}_{36}\overline{\widetilde{\mathfrak{F}}}_{\mathbb{x}}(t)\\&+\mathbb{k}_{37}\overline{\widetilde{\mathfrak{F}}}_{\mathbb{y}}(t)+F(t)\\&=\mathbb{m}_{31}\ddot{\overline{\mathscr{U}}}_0(t)+\mathbb{m}_{32}\ddot{\overline{\mathscr{V}}}_0(t)+\mathbb{m}_{33}\ddot{\overline{\mathscr{W}}}_0(t)+\mathbb{m}_{34}\ddot{\overline{\widetilde{\mathfrak{F}}}}_{\mathbb{x}}(t)+\mathbb{m}_{35}\ddot{\overline{\widetilde{\mathfrak{F}}}}_{\mathbb{y}}(t),\end{aligned} \tag{20c}$$

$$\begin{aligned}&\mathbb{k}_{41}\overline{\mathscr{U}}_0(t)+\mathbb{k}_{42}\overline{\mathscr{V}}_0(t)+\mathbb{k}_{43}\overline{\mathscr{W}}_0(t)+\mathbb{k}_{44}\overline{\mathscr{W}}_0^2(t)+\mathbb{k}_{45}\overline{\widetilde{\mathfrak{F}}}_{\mathbb{x}}(t)+\mathbb{k}_{46}\overline{\widetilde{\mathfrak{F}}}_{\mathbb{y}}(t)\\&=\mathbb{m}_{41}\ddot{\overline{\mathscr{U}}}_0(t)+\mathbb{m}_{42}\ddot{\overline{\mathscr{V}}}_0(t)+\mathbb{m}_{43}\ddot{\overline{\mathscr{W}}}_0(t)+\mathbb{m}_{44}\ddot{\overline{\widetilde{\mathfrak{F}}}}_{\mathbb{x}}(t)+\mathbb{m}_{45}\ddot{\overline{\widetilde{\mathfrak{F}}}}_{\mathbb{y}}(t),\end{aligned} \tag{20d}$$

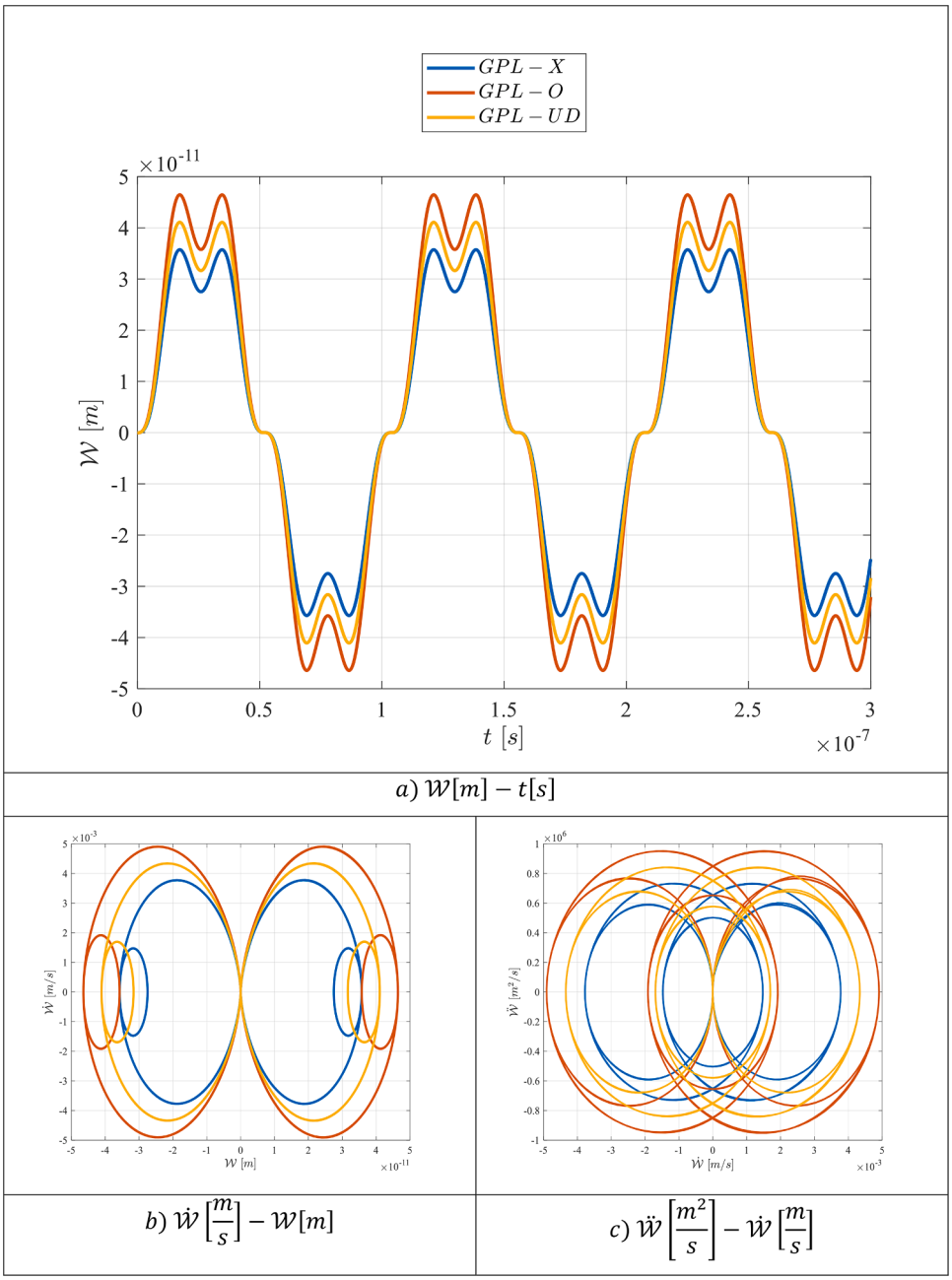

Fig. 4. The impact of GPLs' distribution pattern on the $\mathscr{W}-t$, $\dot{\mathscr{W}}-\mathscr{W}$, and $\ddot{\mathscr{W}}-\dot{\mathscr{W}}$ diagrams of the improved silicon solar cells under external excitation.

$$\begin{aligned}&\mathbb{k}_{51}\overline{\mathscr{U}}_0(t)+\mathbb{k}_{52}\overline{\mathscr{V}}_0(t)+\mathbb{k}_{53}\overline{\mathscr{W}}_0(t)+\mathbb{k}_{54}\overline{\mathscr{W}}_0^2(t)+\mathbb{k}_{55}\overline{\mathscr{S}}_{\mathbb{x}}(t)+\mathbb{k}_{56}\overline{\mathscr{S}}_{\mathbb{y}}(t)\\&=\mathbb{m}_{51}\ddot{\overline{\mathscr{U}}}_0(t)+\mathbb{m}_{52}\ddot{\overline{\mathscr{V}}}_0(t)+\mathbb{m}_{53}\ddot{\overline{\mathscr{W}}}_0(t)+\mathbb{m}_{54}\ddot{\overline{\mathscr{S}}}_{\mathbb{x}}(t)+\mathbb{m}_{55}\ddot{\overline{\mathscr{S}}}_{\mathbb{y}}(t),\end{aligned}\tag{20e}$$

The present analysis makes the assumption that the plate's initial displacements and velocities from nonlinear forced vibration are zero, hence one obtains

$$T|_{t=0}=0, T_{,t}|_{t=0}=0.\left(T=\overline{\mathscr{U}}_0,\ \overline{\mathscr{V}}_0,\ \overline{\mathscr{W}}_0,\ \overline{\mathscr{S}}_{\mathbb{x}},\ \overline{\mathscr{S}}_{\mathbb{y}}\right).\tag{21}$$

By resolving Eqs. (20a)–(20e), the composite plate's nonlinear forced vibration behaviors may be obtained. It is discovered that Eqs. (20a)–(20e) include the in-plane, rotational, and transverse inertia terms. The analytical solutions to Eqs. (20a)–(20e) are very challenging, if not impossible, to acquire. Consequently, the Runge–Kutta technique [40] is used, which is an effective approach, to get the numerical solution of Eqs. (20a)–(20e).

4.2. Linear wave propagation

We assume the following expression

$$\mathscr{U}_0=\overline{\mathscr{U}}_0e^{i\left(K_{\mathbb{x}}\mathbb{x}+K_{\mathbb{y}}\mathbb{y}-\omega t\right)},$$

$$\mathscr{V}_0=\overline{\mathscr{V}}_0e^{i\left(K_{\mathbb{x}}\mathbb{x}+K_{\mathbb{y}}\mathbb{y}-\omega t\right)},$$

$$\mathscr{W}_0=\overline{\mathscr{W}}_0e^{i\left(K_{\mathbb{x}}\mathbb{x}+K_{\mathbb{y}}\mathbb{y}-\omega t\right)},$$

$$\mathscr{S}_{\mathbb{x}}=\overline{\mathscr{S}}_{\mathbb{x}}e^{i\left(K_{\mathbb{x}}\mathbb{x}+K_{\mathbb{y}}\mathbb{y}-\omega t\right)},$$

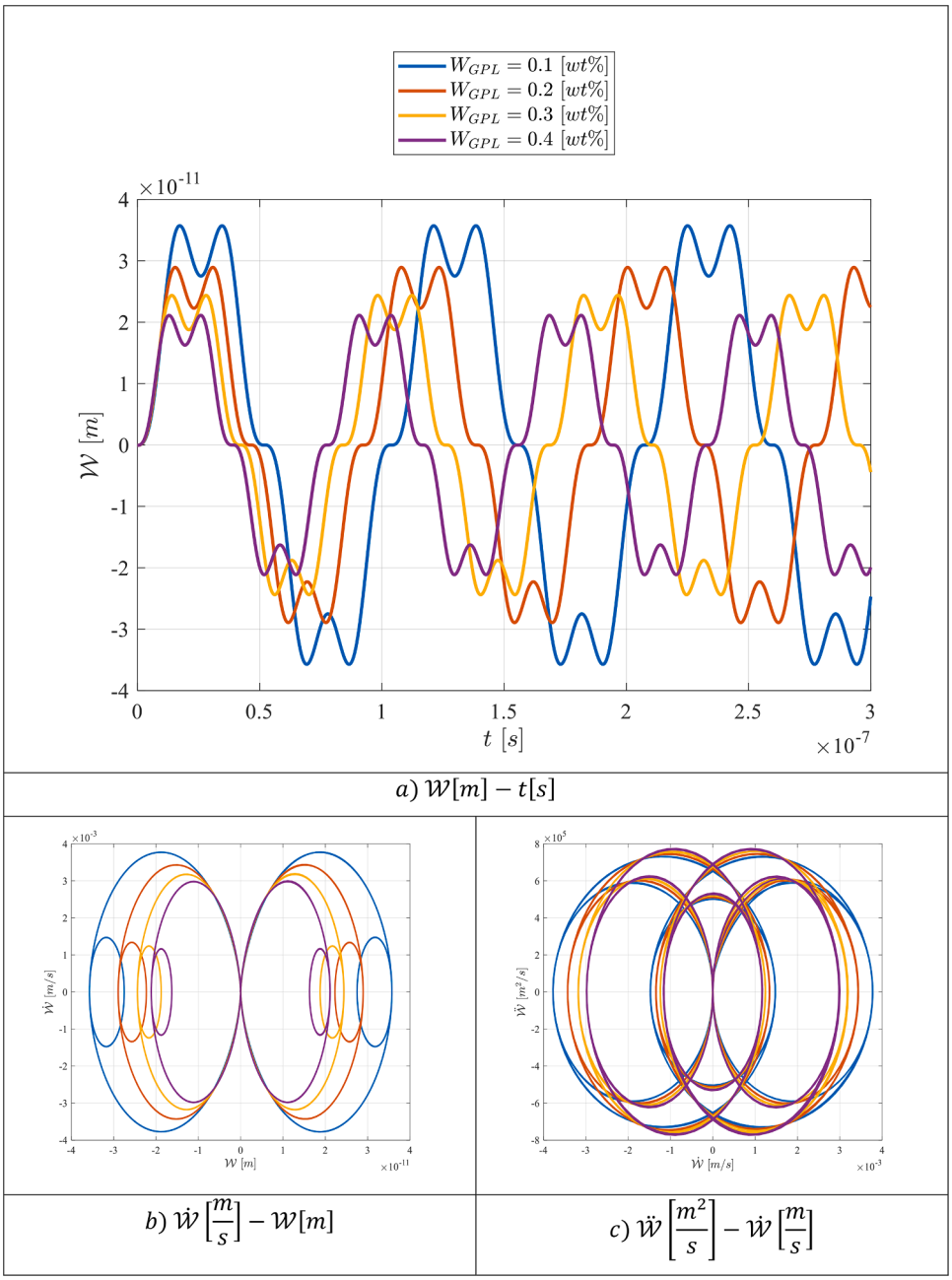

Fig. 5. The impact of GPLs' weight fraction on the $\mathscr{W} - t$, $\dot{\mathscr{W}} - \mathscr{W}$, and $\ddot{\mathscr{W}} - \dot{\mathscr{W}}$ diagrams of the improved silicon solar cells under external excitation.

$$\mathfrak{F}_{\mathbb{y}} = \overline{\mathfrak{F}}_{\mathbb{y}} e^{i\left(K_{\mathbb{x}}\mathbb{x} + K_{\mathbb{y}}\mathbb{y} - \omega t\right)}. \tag{22}$$

where $\overline{\mathscr{U}}_0$, $\overline{\mathscr{V}}_0$, $\overline{\mathscr{W}}_0$, $\overline{\mathfrak{F}}_{\mathbb{x}}$, and $\overline{\mathfrak{F}}_{\mathbb{y}}$ introduces for the wave amplitudes; ω represents the wave frequency; K_x, and K_y are defined to determine the wave numbers. The eigenvalue equation is obtained by substituting Eq. (22) into Eqs. (18a–e) and then eliminating the nonlinear components and external load.

$$\left([\mathbb{m}] - \omega^2[\mathbb{k}]\right)\{\Delta\} = 0, \tag{23}$$

where $\{\Delta\} = \left\{\overline{\mathscr{U}}_0 \quad \overline{\mathscr{V}}_0 \quad \overline{\mathscr{W}}_0 \quad \overline{\mathfrak{F}}_{\mathbb{x}} \quad \overline{\mathfrak{F}}_{\mathbb{y}}\right\}^T$, the stiffness matrix and mass matrix are characterized by $[\mathbb{k}]$ and $[\mathbb{m}]$, respectively.

Also, the phase velocity can be calculated by Eq. (24)

$$\textit{Phase velocity} = \frac{\omega}{K_x} \tag{24}$$

5. DNN Combined with GA as a bio-inspired optimization approach to predict nonlinear wave propagation in silicon solar cells

The demand for more efficient energy conversion devices has sparked significant interest in understanding the behavior of silicon solar cells under various conditions, including nonlinear wave propagation. In photovoltaic systems, nonlinearities arise from multiple factors, including material properties, geometrical configurations, and operational conditions. Accurate prediction and analysis of nonlinear wave propagation in silicon solar cells are critical for improving their performance, durability, and operational efficiency. Traditional computational methods, although effective in capturing linear wave behavior, often fall short in predicting the complexities involved in nonlinear wave propagation. This limitation has driven researchers toward advanced modeling techniques, particularly artificial intelligence

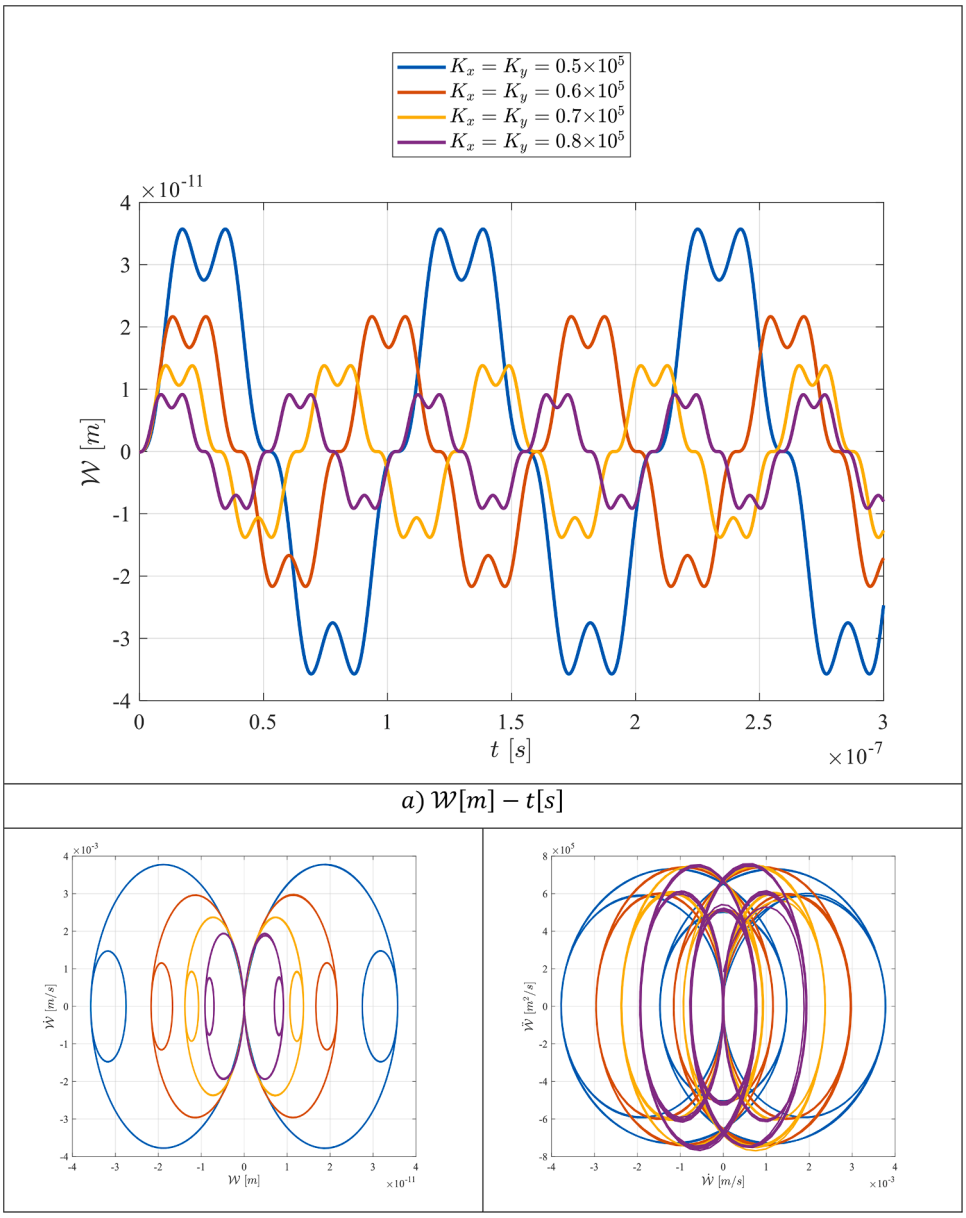

Fig. 6. The impact of wave numbers along with various directions on the $\mathcal{W} - t$, $\dot{\mathcal{W}} - \mathcal{W}$, and $\ddot{\mathcal{W}} - \dot{\mathcal{W}}$ diagrams of the improved silicon solar cells under external excitation.

(AI) approaches. DNN has emerged as powerful tools in handling complex nonlinear systems due to their ability to learn intricate patterns and relationships from data. When combined with a genetic algorithm (GA), which is a bio-inspired optimization technique, these two methods offer a synergistic approach for solving nonlinear wave propagation problems. A DNN-GA hybrid algorithm leverages the learning capabilities of DNN and the evolutionary search mechanisms of GA to optimize the parameters governing wave propagation in silicon solar cells. The genetic algorithm mimics natural selection processes, making it an effective optimization tool for navigating large and complex search spaces. It enhances the predictive accuracy of DNN by iteratively refining its weights and biases based on fitness evaluation, mutation, and crossover techniques, thus optimizing the model to capture nonlinear behaviors with greater precision. The DNN-GA approach is particularly useful in predicting nonlinearities in the wave propagation of silicon solar cells, where traditional physics-based models may struggle. By combining the best of AI and evolutionary algorithms, this bio-inspired optimization method facilitates the accurate prediction of nonlinear wave behavior. The approach not only reduces computational costs but also improves prediction accuracy, offering a more efficient means of analyzing and optimizing the performance of solar cells under various environmental and operational conditions. The DNN-GA hybrid algorithm offers several advantages over traditional algorithms and other artificial intelligence methods, particularly in the context of predicting nonlinear wave propagation in silicon solar cells:

1. **Enhanced Accuracy for Complex Nonlinear Systems**
   Traditional methods such as finite element analysis or classical machine learning models often struggle with capturing highly nonlinear behavior, especially in complex systems like wave propagation in solar cells. The DNN-GA algorithm can better handle such nonlinearity by leveraging deep learning's ability to learn complex patterns and genetic algorithms' ability to optimize solutions across large search spaces.
2. **Optimization of Model Parameters**
   One of the major advantages of combining DNN with GA is the

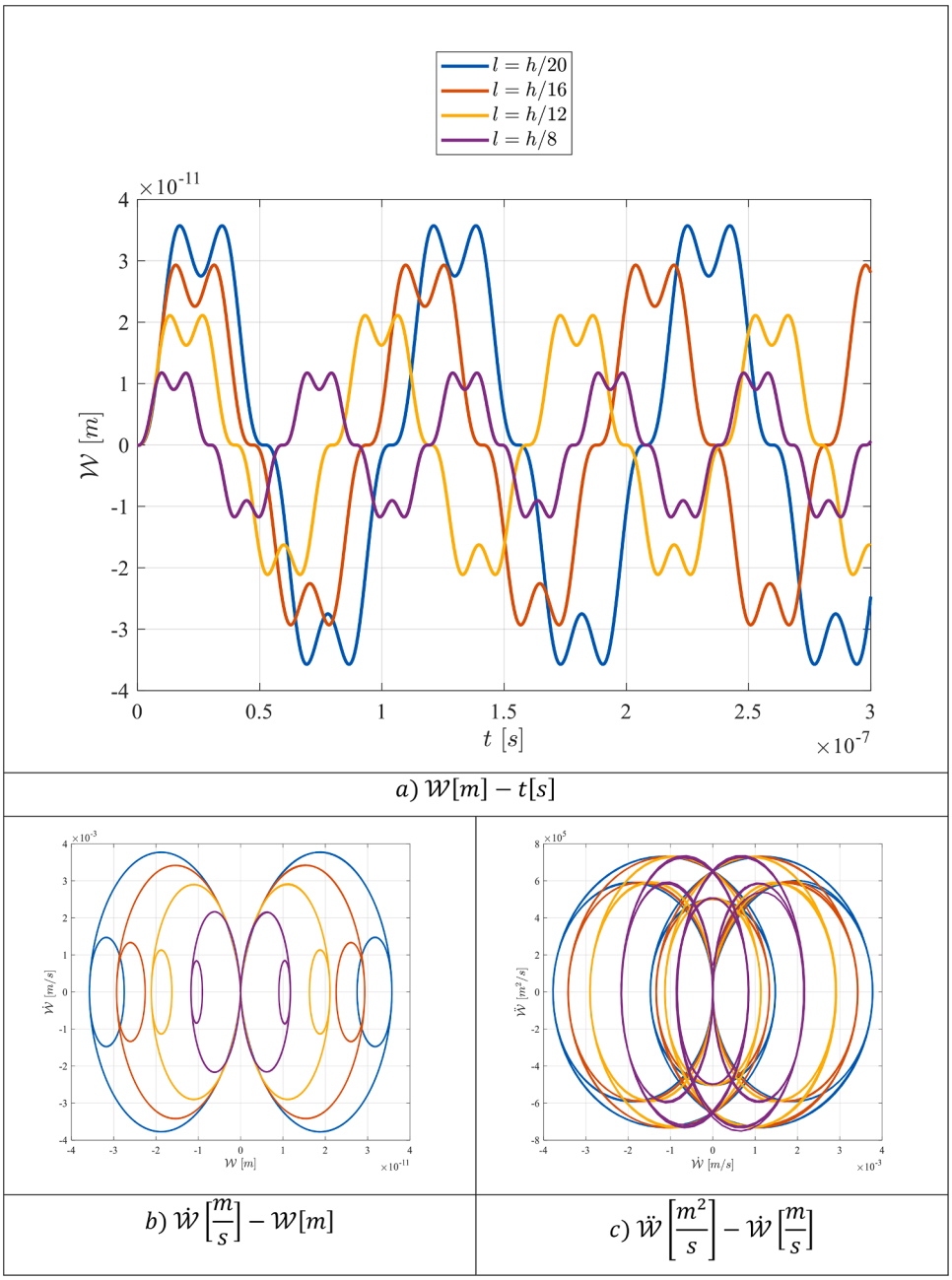

Fig. 7. The impact of length scale parameter on the $\mathcal{W} - t$, $\dot{\mathcal{W}} - \mathcal{W}$, and $\ddot{\mathcal{W}} - \dot{\mathcal{W}}$ diagrams of the improved silicon solar cells under external excitation.

ability to optimize the neural network's architecture and hyperparameters. GA helps find the optimal weights, biases, and network configurations, improving the predictive performance of the model and ensuring that it captures essential nonlinear dynamics more effectively than standard optimization techniques such as gradient descent alone.

3. **Bio-Inspired Adaptability**
   The genetic algorithm component of DNN-GA is bio-inspired and mimics the process of natural selection. This adaptability allows it to explore a broader solution space and avoid local minima traps that other optimization algorithms, like gradient-based approaches, might encounter. It is particularly useful in dynamic or multi-objective environments, making it more robust for complex solar cell models where nonlinear interactions vary significantly with changing conditions.
4. **Faster Convergence in High-Dimensional Spaces**
   When working with high-dimensional data, such as in wave propagation scenarios, traditional methods may struggle with slow convergence and high computational costs. The DNN-GA algorithm, by intelligently selecting and evolving promising candidates, can find near-optimal solutions faster than many other algorithms, reducing the computational time and resources required for complex simulations.
5. **Handling of Multi-Modal Solutions**
   Nonlinear wave propagation problems often exhibit multiple solutions or modes of behavior. The genetic algorithm is designed to handle multi-modal optimization problems effectively, ensuring that the DNN-GA hybrid can find global optima where other algorithms might converge prematurely to suboptimal solutions.
6. **Scalability and Flexibility**
   The DNN-GA algorithm is highly scalable and can be adapted to

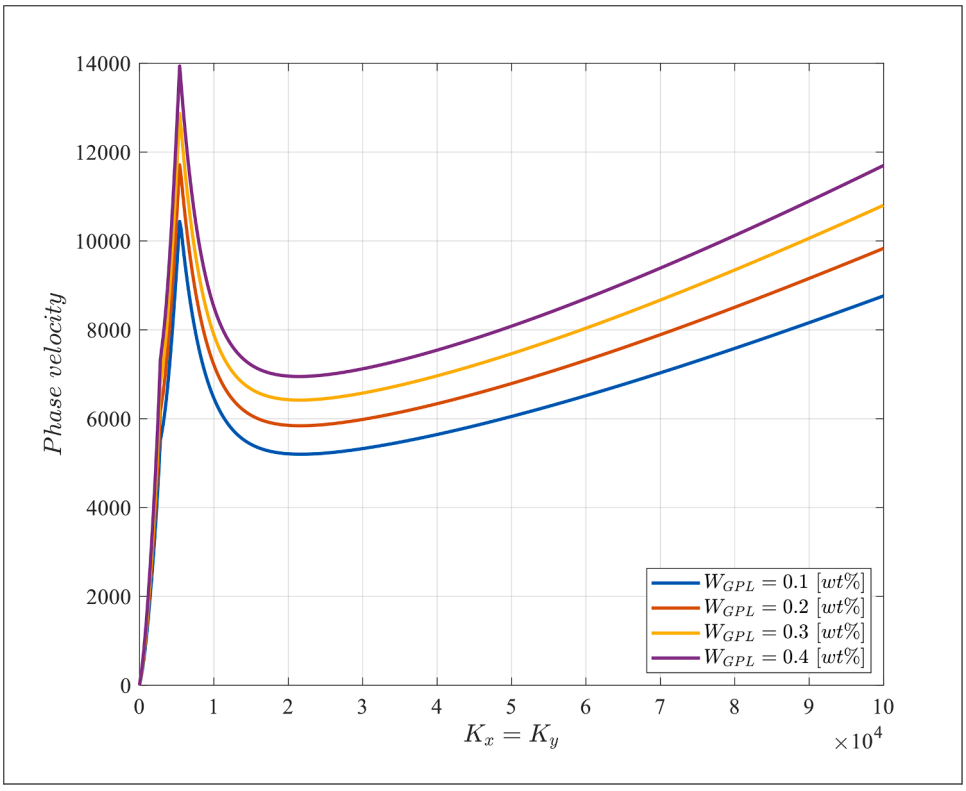

Fig. 8. The impact of GPLs' weight fraction on the phase velocity information of the improved silicon solar cells under external excitation for various wave numbers.

various problem sizes and configurations. Whether the system involves small-scale wave propagation in microstructures or large-scale solar arrays, the algorithm's flexibility makes it suitable for a wide range of applications, unlike more rigid or problem-specific models.

7. **Improved Generalization**
   By combining DNN's capacity for learning complex, generalized representations of data with GA's optimization abilities, the hybrid algorithm tends to generalize better on unseen data compared to purely data-driven models. This is crucial for accurately predicting the performance of solar cells under diverse operating conditions that were not explicitly included in the training data.
8. **Reduced Risk of Overfitting**
   Overfitting is a common problem in deep learning, where models perform well on training data but poorly on new, unseen data. The evolutionary search process of the GA can help mitigate this by regularly introducing variations during the optimization process, preventing the model from becoming too fine-tuned to specific data sets.

These advantages make the DNN-GA algorithm particularly well-suited for complex, nonlinear problems like wave propagation in silicon solar cells, where other algorithms might fall short in terms of accuracy, convergence, or adaptability. Fig. 3 shows a MATLAB implementation of the hybrid algorithm combining a deep neural network with a genetic algorithm for predicting nonlinear wave propagation. This code demonstrates how the GA optimizes the weights and biases of a simple neural network model.

The hybrid algorithm combining a **DNN** with a **GA,** referred to as **DNN-GA**, can be mathematically formulated by integrating the principles of both methods.

5.1. Neural Network Formulation

A **feedforward neural network** (DNN) maps an input vector $x \in R^n$ to an output vector $y \in R^m$. The neural network consists of multiple layers, each containing a set of neurons. The relationship between the input and output is defined by weights and biases, optimized using the GA.

Let's consider a simple feedforward network with L layers.

- W_l and b_l represent the weights and biases of the $l-th$ layer.
- $\sigma(\cdot)$ represents the activation function (e.g., ReLU, sigmoid).
- h_l is the output of the $l-th$ layer (also referred to as activations).

For the $l-th$ layer, the transformation can be written as:

$$h_l = \sigma(W_l h_{l-1} + b_l) \tag{25}$$

where:

- $h_0 = x$ is the input vector.
- $h_L = y$ is the predicted output.

The final predicted output y_{pred} of the DNN after L layers is given by:

$$y_{pred} = h_L = W_L\sigma(W_{L-1}\sigma(\ldots\sigma(W_L x + b_1)\ldots) + b_{L-1}) + b_L. \tag{26}$$

The loss function, typically Mean Squared Error (MSE), measures the difference between the predicted output y_{pred} and the true output y_{true}:

$$Loss = \frac{1}{N}\sum_{i=1}^{N}\left(y_{pred,i} - y_{true,i}\right)^2. \tag{27}$$

where N is the number of training samples.

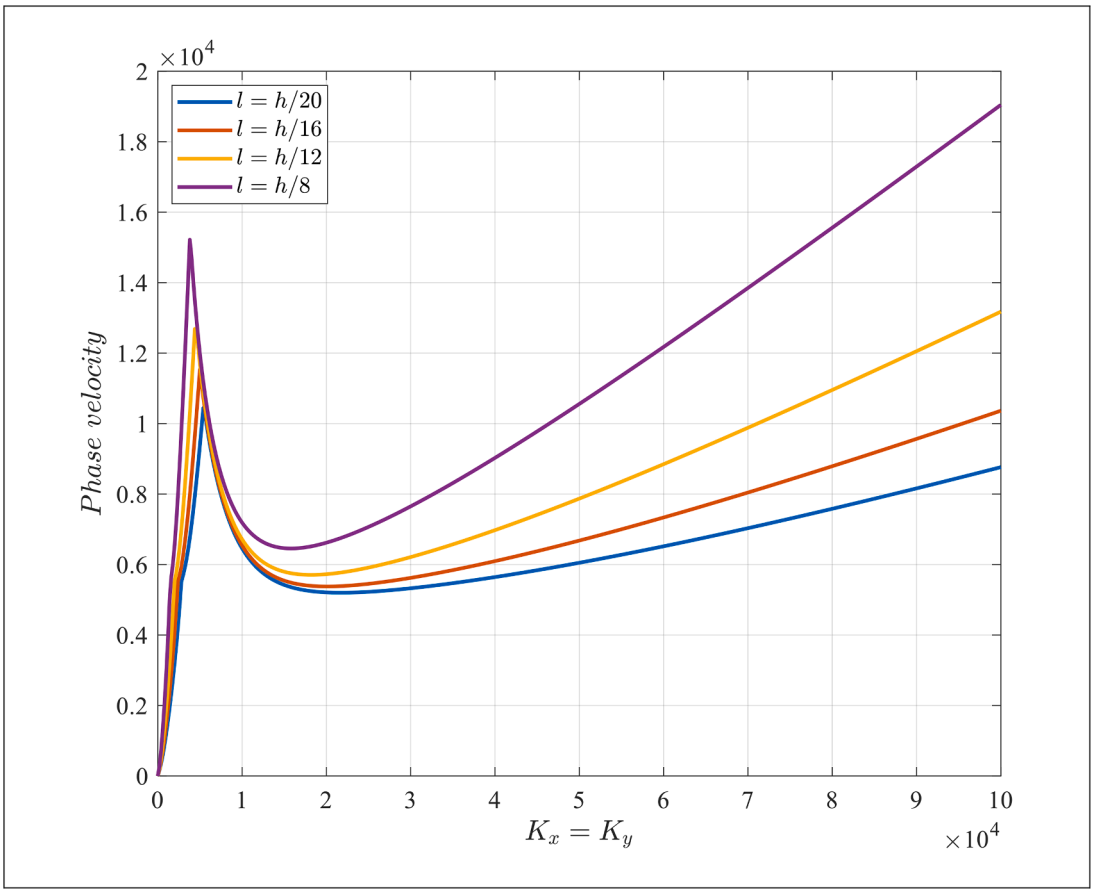

Fig. 9. The impact of length scale parameter on the phase velocity information of the improved silicon solar cells under external excitation for various wave numbers.

5.2. Genetic Algorithm Formulation

The Genetic Algorithm (GA) is a bio-inspired optimization technique used to minimize the loss function by optimizing the weights and biases W_L and b_L of the neural network.

The GA operates as follows:

a. **Chromosome Representation**

Each individual in the GA population represents a set of neural network weights and biases, encoded as a chromosome. The chromosome c_i for the $i-th$ individual is a flattened vector that combines all weights and biases:

$$c_i = [W_1, b_1, W_2, b_2, \ldots, W_1, b_1]. \tag{28}$$

b. **Fitness Function**

The fitness function evaluates the performance of each individual (chromosome) based on how well the neural network predicts the output. The fitness is inversely related to the loss function (e.g., MSE):

$$Fitness(c_i) = \frac{1}{Loss(c_i) + \epsilon}. \tag{29}$$

where ϵ is a small number to avoid division by zero.

c. **Selection**

The GA selects the best-performing individuals (chromosomes) based on their fitness scores. The selection can be done using techniques such as roulette wheel selection or tournament selection.

d. **Crossover**

Crossover generates new offspring by combining the genetic information (weights and biases) from two parent chromosomes c_i and c_j. The most common crossover technique is single-point crossover, where a random crossover point is selected, and the chromosomes are split and recombined:

$$c_{offspring} = [c_i(1 : cross\_point),\ c_j(cross\_point + 1 : end). \tag{30}$$

e. **Mutation**

Mutation introduces small random changes to the genes (weights and biases) of the offspring, ensuring diversity in the population and helping the algorithm escape local minima. Each gene in the chromosome has a small probability P_{mut} of being mutated:

$$c_{mutated}(k) = c_{offspring}(k) + \delta. \tag{31}$$

where δ is a small random perturbation.

f. **Next Generation**

After crossover and mutation, a new population of chromosomes is generated, and the process is repeated for several generations until convergence or a maximum number of generations is reached.

5.3. DNN-GA Algorithm Flow

The overall DNN-GA algorithm combines the deep learning model (DNN) with GA optimization and follows these steps:

· **Initialization**:

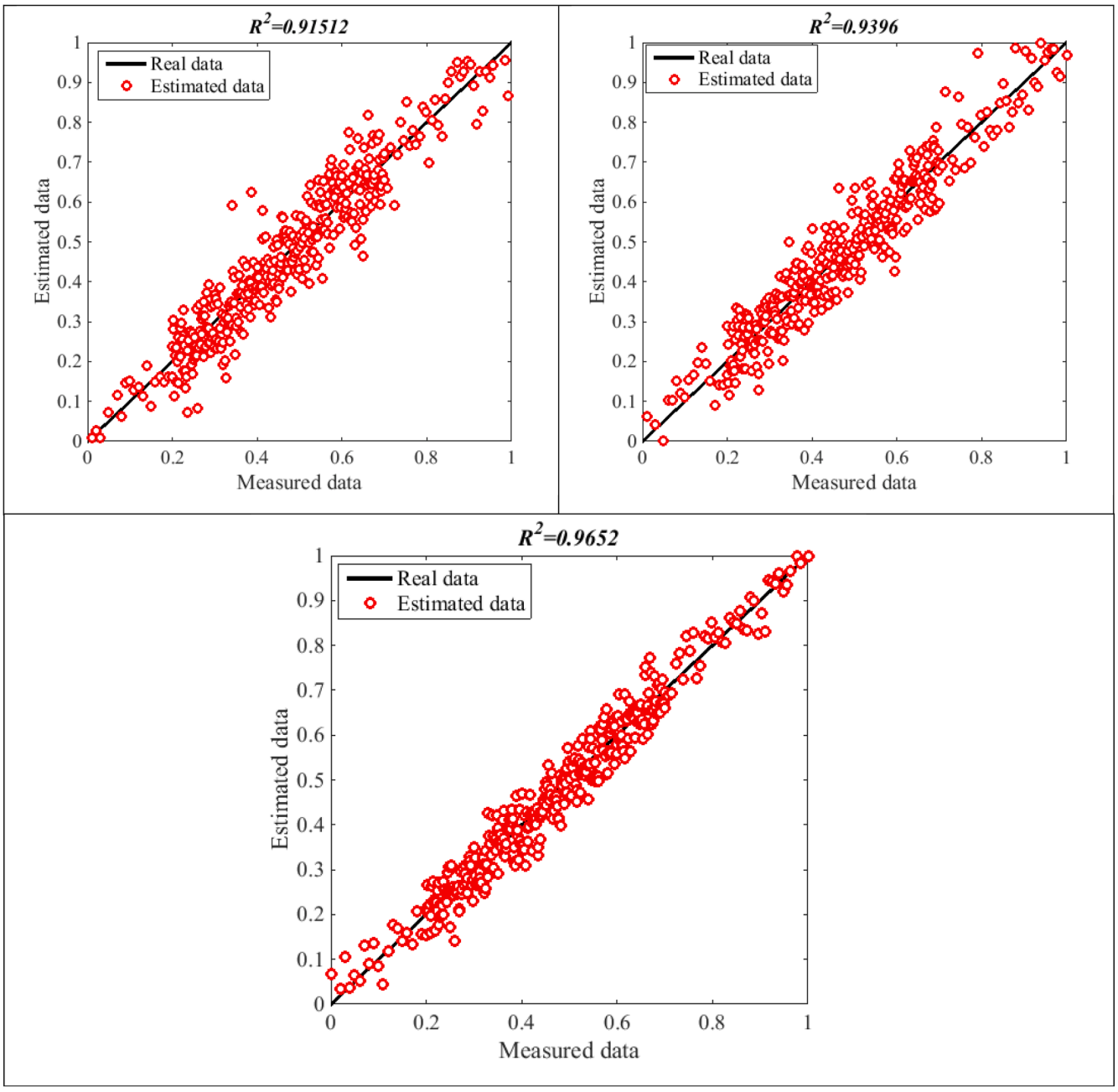

Fig. 10. The performance of a predictive model in terms of its estimated data versus measured data across three different scenarios.

- Randomly initialize the population of chromosomes $C = \{c_1, c_2, \ldots, c_{pop\_size}\}$.
- Set the number of generations and other GA parameters (e.g., mutation rate).

· **Evaluate Fitness**:

- For each chromosome c_i, set the neural network weights and biases using c_i.
- Calculate the fitness using the loss function on the training dataset.

· **Selection**:

- Select the best-performing individuals (parents) based on their fitness scores.

· **Crossover**:

- Perform crossover between selected parents to generate offspring.

· **Mutation**:

- Mutate some genes in the offspring chromosomes to introduce diversity.

· **Create Next Generation**:

- Replace the old population with the new population of parents and offspring.

· **Repeat**:

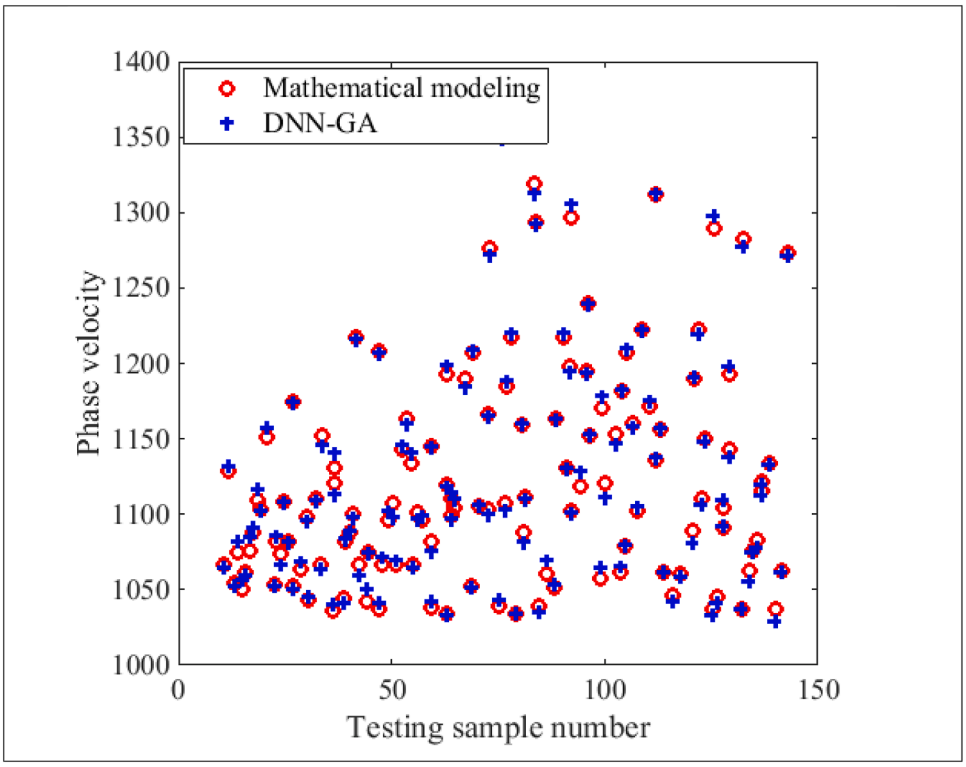

Fig. 11. The phase velocity predictions obtained from DNN-GA and mathematical modeling across different testing samples.

- Repeat steps 2 to 6 for a fixed number of generations or until convergence.

· **Final Solution**:

- The best chromosome in the final population represents the optimized neural network with the best weights and biases.

6. Result and discussion

6.1. Validation

Table 3 presents a comparative analysis of circular frequency (ω) results between the current study and those reported in Ref. [41], for various wavenumbers. The wavenumbers evaluated range from 2 to 14, providing insight into how the circular frequencies behave across different propagation conditions. The first row, labeled "Present," lists the results from the current study. For a wavenumber of 2, the circular frequency is 128.24, increasing progressively with the wavenumber to reach a value of 6239.88 at $K_x = K_y = 14$. These results are compared with those from Ref. [41], shown in the second row. The circular frequencies in Ref. [41] are similar to the present study, with a circular frequency of 128.26 at a wavenumber of 2, and 6240.55 at a wavenumber of 14. The small discrepancies between the values are likely attributable to numerical precision or slight methodological differences in calculating the circular frequencies. However, the close agreement across all wavenumbers confirms the accuracy and reliability of the present results. This table reinforces that the model and approach adopted in the current study are consistent with established methods in the literature for analyzing the dynamic behavior of wave propagation in advanced materials, such as those used in improved silicon solar cells.

6.2. Parametric study

Fig. 4 presents the analysis of **nonlinear guided waves** in **improved silicon solar cells** under external excitation, focusing on the impact of **GPLs** distribution patterns on system response. The figure is divided into three subplots. **Subplot 4a** illustrates the variation of $\mathscr{W}$ over time. It shows the system's response under three different distribution patterns of GPLs, labeled as **GPL-X, GPL-0**, and **GPL-UD**. The x-axis represents time, while the y-axis shows the displacement $\mathscr{W}$ in meters. The displacement exhibits a periodic behavior with peaks and valleys, highlighting the effect of external excitation. The response for each GPL distribution pattern varies slightly, with **GPL-UD** showing the highest amplitude, followed by **GPL-0** and **GPL-X**. This variation demonstrates how the GPL distribution affects the mechanical response of the solar

Table 4
Key parameters used in both the neural network and the genetic algorithm.

Parameter	Description	Value
Input Size	Number of input features	6
Output Size	Number of outputs	3
Number of Hidden Layers	Layers between input and output	4
Neurons per Hidden Layer	Number of neurons in each hidden layer	64
Activation Function	Nonlinear function applied at each neuron	ReLU
Population Size	Number of chromosomes in GA population	20
Number of Generations	Iterations of evolution	50
Number of Parents	Number of top performers selected as parents	10
Crossover Rate	Probability of crossover	0.8
Mutation Rate	Probability of mutation	0.1
Crossover Type	Method of combining parent genes	Single-point crossover
Mutation Type	Method of introducing random changes	Add small perturbations
Fitness Function	Inverse of loss function (MSE)	1/MSE
Termination Criteria	Condition to stop GA evolution	Fixed number of generations

cell under dynamic loading. **Subplot 4b** is a phase-space plot, representing the relationship between the $\ddot{\mathscr{W}}$ and its $\dot{\mathscr{W}}$. The trajectories form closed loops, typical of nonlinear oscillatory systems. Each loop corresponds to a different GPL distribution pattern, and the differences in the loop shapes show how the system's energy dissipation and dynamic response are influenced by the GPL configuration. The **GPL-UD** configuration produces the largest loop, indicating a more significant dynamic response compared to the other patterns. **Subplot 4c** shows the phase-space plot of the $\ddot{\mathscr{W}}$ versus velocity $\dot{\mathscr{W}}$. The intertwined loops for the different GPL patterns further illustrate the nonlinear characteristics of the system. Again, the **GPL-UD** pattern results in the largest loop size, indicating a more pronounced effect on the system's acceleration.

Fig. 5 illustrates the dynamic behavior of silicon solar cells in the presence of graphene platelets under external excitation. This figure is divided into three subplots. Subplot 5a demonstrates the temporal response of the deflection of the solar cells, with respect to time, for different weight fractions of GPLs (0.1, 0.2, 0.3, and 0.4 *wt*%). Each colored curve corresponds to a specific GPL weight fraction. The graph shows increasing oscillatory behavior as the GPL fraction rises, indicating that the nonlinear guided wave responses become more complex with higher fractions of GPLs. The peak amplitudes of deflections are slightly amplified with increasing GPL content, suggesting a more significant dynamic influence on the system's response. Subplot 5b presents a phase-space diagram showing the relationship between velocity and displacement. The closed, oval-shaped trajectories indicate periodic motion, with distinct loops corresponding to different GPL weight fractions. The figure highlights that increasing the GPL content affects the overall shape and size of these loops, suggesting an alteration in the system's energy dissipation and stability behavior. Subplot 5c illustrates the relationship between acceleration and velocity), revealing the system's vibrational dynamics. The overlapping elliptical curves reflect nonlinear interactions, where higher GPL content leads to broader, more complex trajectories. In summary, this figure captures the nonlinear dynamic responses of improved silicon solar cells, showing that an increase in GPLs' weight fraction leads to more pronounced and complex vibrational characteristics under external excitation.

Fig. 6 illustrates the dynamic response of silicon solar cells subject to different wave numbers along multiple directions under external excitation. The figure consists of three subplots. Subplot 6a shows the temporal response of the deflection of the solar cells with respect to time for varying wave numbers. The oscillations presented by each colored curve reflect how different wave numbers influence the dynamic response of the system. As the wave numbers increase, the deflection patterns exhibit heightened complexity, suggesting that higher wave numbers amplify the system's oscillatory behavior under the applied external excitation. Subplot 6b presents a phase-space diagram that explores the relationship between velocity and displacement. The graph shows various elliptical orbits, indicating periodic or quasi-periodic motion within the system. The size and shape of the ellipses vary based on the wave numbers, showing a noticeable shift in the dynamical properties of the system as wave numbers increase, likely due to changes in energy dissipation and wave propagation characteristics. Subplot 6c depicts the relationship between acceleration and velocity, showing complex overlapping curves. This phase-space diagram shows how the interplay between acceleration and velocity evolves with different wave numbers, leading to more intricate trajectories as the wave numbers increase. The denser loops indicate stronger nonlinearities in the response. In summary, the figure illustrates that varying wave numbers significantly influence the nonlinear dynamic behavior of improved silicon solar cells, with higher wave numbers resulting in more pronounced and complex oscillatory patterns under external excitation.

Fig. 7 highlights the effect of varying length scale parameters on the dynamic behavior of silicon solar cells. The figure contains three subplots. Subplot 7a shows the time evolution of deflection for different length scale. The curves indicate how the response of the solar cells varies over time under external excitation. As the length scale increases, the oscillatory behavior becomes more amplified, with the magnitude and frequency of deflection increasing, indicating stronger wave propagation and interaction. Subplot 7b is a phase-space plot that correlates velocity with displacement. The elliptical trajectories change in size and shape as the length scale parameter increases, demonstrating how this parameter influences the periodicity and energy distribution in the system. Subplot 7c shows the relationship between acceleration and velocity. The denser, more complex curves with increasing length scales suggest a more pronounced nonlinearity in the system's vibrational response. Overall, the figure demonstrates that larger length scale parameters lead to more complex, amplified dynamic behaviors in the improved silicon solar cells under external excitation.

Fig. 8 illustrates the relationship between phase velocity and wavenumber for improved silicon solar cells with varying graphene platelets weight fractions, ranging from 0.1 *wt*% to 0.4 *wt*%. The phase velocity is plotted on the y-axis, while the wavenumber $K_x = K_y$ is on the x-axis, ranging from 0 to 10^4. As the weight fraction of GPLs increases, the phase velocity increases as well, indicating that the incorporation of GPLs enhances the material's ability to support faster wave propagation. Initially, all curves exhibit a steep rise in phase velocity for small wavenumbers, reaching a peak before experiencing a significant drop as wavenumber increases. This indicates a resonance-like behavior at low wavenumbers. Beyond this drop, the phase velocity starts to increase again with further increases in wavenumber, showing a stabilization trend at higher values of wavenumber. The magnitude of the peak and the subsequent values of phase velocity are higher for samples with larger weight fractions of GPLs, which indicates the strengthening effect of GPL reinforcement on the silicon solar cells. The results suggest that a higher concentration of GPLs enhances the stiffness and the dynamic response of the composite, resulting in greater phase velocities. This behavior is critical for applications where guided wave propagation plays a role, as faster phase velocities can improve the efficiency of energy transfer in the solar cells, making them more effective under external excitations. This figure emphasizes the importance of GPL weight fraction in optimizing the performance of these improved silicon solar cells.

Fig. 9 demonstrates the effect of the length scale parameter on the phase velocity of improved silicon solar cells under external excitation for different wavenumbers. The phase velocity is shown on the y-axis, while the wavenumber is plotted on the x-axis. Various curves represent different length scale parameters l, normalized by the plate thickness h, with values ranging from $l = h/20$ to $l = h/8$. Similar to the previous figure, all the curves exhibit an initial rise in phase velocity at small wavenumbers, followed by a rapid drop, after which the phase velocity gradually increases as the wavenumber continues to rise. The magnitude of both the peak and subsequent phase velocities is influenced by the length scale parameter. Larger length scale parameters, such as $l = h/8$, result in higher phase velocities across the entire wavenumber range, suggesting that the size of the structural elements in relation to the thickness of the cell plays a critical role in determining the wave propagation characteristics. The curves indicate that as the length scale parameter increases, the material becomes stiffer, allowing for faster wave propagation at both low and high wavenumbers. The resonance-like peak observed at lower wavenumbers shows a shift in amplitude based on the length scale, indicating that the cell's dynamic response is highly sensitive to its geometry. These results highlight the importance of optimizing the length scale parameter when designing silicon solar cells for applications involving guided waves, as it directly impacts the efficiency of wave propagation within the material.

6.3. The outcomes of the mentioned algorithm

Fig. 10 provided shows the performance of a predictive model in terms of its estimated data versus measured data across three different scenarios. Each plot includes the coefficient of determination, R^2, which

quantifies how well the estimated values fit the measured data. The R^2 values in these plots—0.91512, 0.9396, and 0.9652—indicate that the model performs well in all cases, with a higher R^2 value representing a stronger fit between the predicted and measured data. This performance suggests that the model in question is highly capable of making accurate predictions. In this context, the algorithm used is a combination of a **DNN** and a **GA**, referred to as **DNN-GA**, which integrates machine learning with bio-inspired optimization. How the algorithm works:

1. **DNN**: The DNN is the core prediction model, structured with an input layer, multiple hidden layers, and an output layer. It learns patterns from the input data through nonlinear transformations in the hidden layers. Each layer applies a weighted combination of inputs followed by an activation function (e.g., ReLU, sigmoid), gradually adjusting weights through the training process to minimize error.
2. In this algorithm, the DNN is trained to approximate nonlinear functions—such as predicting the response of a solar cell under nonlinear wave propagation. The neural network learns the relationship between the input features (e.g., physical parameters of the solar cell, wave properties) and the output (e.g., displacement, stress, or energy response).
3. **GA**: GA is an evolutionary optimization technique used to improve the performance of the DNN. The GA optimizes the weights and biases of the neural network by mimicking natural selection. It starts with an initial population of random weight configurations, and through selection, crossover, and mutation, it generates new populations over successive generations. The fitness of each individual (chromosome) is evaluated based on how well the corresponding neural network performs on the task, as measured by its R^2 value or mean squared error (MSE).
4. **Optimization Flow**:
   - **Initialization**: The GA initializes the weights and biases randomly.
   - **Training DNN**: For each set of weights, the DNN is trained and evaluated.
   - **Fitness Evaluation**: The GA calculates the fitness of each chromosome based on the error between the predicted and real data (in this case, visualized in the plot).
   - **Selection and Reproduction**: The best-performing networks (those with higher R^2) are selected as parents to produce offspring through crossover and mutation. These new weight configurations are then tested in the next generation.
   - **Convergence**: This process continues for several generations until the model reaches an optimal configuration of weights and biases that minimizes the error.

As mentioned in Fig. 10, the high R^2 values in the plots reflect the model's predictive capability, showing that the DNN-GA algorithm effectively captures the underlying nonlinear behavior of the system being modeled. For instance, the R^2 values of 0.91512, 0.9396, and 0.9652 suggest that the majority of the variance in the measured data is explained by the model's predictions, indicating a high level of accuracy in estimating the system's response. By combining the learning power of deep neural networks with the optimization strength of genetic algorithms, this approach leverages both gradient-based learning and evolutionary search, allowing for highly accurate predictions in complex systems like nonlinear wave propagation in silicon solar cells.

Fig. 11 compares the phase velocity predictions obtained from DNN-GA and mathematical modeling across different testing samples. The x-axis represents the testing sample number (ranging from 0 to 150), and the y-axis represents the phase velocity in a range from 1000 to 1400 units. The red circles in the plot indicate the results from mathematical modeling, while the blue plus signs represent the predictions from the DNN-GA model. The two sets of points are plotted together, allowing a comparison of how closely the DNN-GA model predicts phase velocity compared to the results from traditional mathematical models. From a general observation of the figure, it is clear that the predictions made by the DNN-GA are very close to those derived from mathematical modeling. In most cases, the blue crosses overlap with or are very close to the red circles, suggesting that the DNN-GA has learned the underlying relationship between the input variables and the phase velocity with high accuracy. The scattered nature of the points reflects the variability in phase velocity across different samples, likely due to differences in the properties of the system (e.g., wave properties or material characteristics) being modeled. This comparison demonstrates the effectiveness of DNN-GA as a predictive tool for phase velocity in complex systems, where it can approximate results from well-established mathematical models. The ability of DNN-GA to capture nonlinearity and generalize from training data allows them to provide accurate predictions, as shown in the figure. It also highlights the DNN-GA's potential to be used as a surrogate model, capable of performing real-time predictions with reduced computational effort compared to more traditional methods. Thus, the figure effectively demonstrates the alignment between DNN-GA predictions and mathematical modeling, suggesting that the DNN-GA can be a reliable tool in predicting phase velocity for complex physical systems.

In the DNN-GA algorithm for predicting nonlinear wave propagation, the key parameters used in both the neural network and the genetic algorithm are outlined in Table 4. These parameters influence both the structure of the neural network and the performance of the optimization process.

7. Conclusion

In this study, the nonlinear guided wave propagation in improved silicon solar cells reinforced by graphene platelet nanocomposites was comprehensively analyzed. The microplate model of the silicon solar cells was developed using the modified couple stress theory, incorporating size-dependent effects, while the sinusoidal shear deformation theory was employed to accurately represent shear deformation. Nonlinear equations governing the dynamic response of the nanocomposite-reinforced solar cells were derived, and the Runge–Kutta method was applied to solve these equations numerically. The study revealed that the inclusion of GPL nanocomposites significantly enhanced the mechanical performance of the silicon solar cells, which resulted in higher phase velocities for guided waves across various wavenumbers. It was demonstrated that increasing the GPL weight fraction improved the material stiffness and overall wave propagation efficiency. The results also highlighted the strong dependence of the phase velocity on the length scale parameter, particularly at low wavenumbers, showing that larger length scale parameters led to a noticeable increase in phase velocity. The findings confirmed that the nonlinear behavior of the guided waves was effectively captured by the coupled framework of MCST and SSDT. Additionally, the Runge–Kutta method proved to be a robust and reliable tool for solving the complex nonlinear equations of motion. In this investigation, an intelligent model based on deep neural networks as an artificial intelligent algorithm combined with a genetic algorithm as a bio-inspired optimization approach, was employed to predict nonlinear phenomena in guided waves within the solar cell, using datasets generated from mathematical simulations. Overall, this research offered important insights into the design and optimization of next-generation silicon solar cells using GPL nanocomposites. By enhancing the phase velocity and improving wave propagation characteristics, the study provided a solid foundation for further developments in solar cell technology where guided waves play a crucial role in performance enhancement. Future work could focus on refining the models to include more complex boundary conditions and additional material properties, expanding the potential applications of these nanocomposite-reinforced solar cells in energy harvesting systems.

CRediT authorship contribution statement

Lei Chang: Investigation, Resources, Software, Validation, Visualization, Writing – review & editing. **Wenqing Yang:** Writing – review & editing, Writing – original draft, Visualization, Validation, Supervision, Software, Resources, Project administration, Investigation. **Mohammed El-Meligy:** Resources, Software, Validation, Visualization, Writing – review & editing. **Khalil El Hindi:** Resources, Validation, Visualization, Writing – review & editing.

Declaration of competing interest

The authors declare that they have no conflict of interest.

Funding

This research was supported by Value-added Research on Decarbonization Technology for Fossil Fuels under China's Energy Security Strategy (grant number Z9TZ4240009) and Scientific Research Foundation for High-level Talents of Anhui University of Science and Technology, China (grant number 2024yjrc37, 2024yjrc36). The authors extend their appreciation to King Saud University for funding this work through Researchers Supporting Project number (RSPD2024R953), King Saud University, Riyadh, Saudi Arabia.

Data availability

Data will be made available on request.

References

[1] R. Verduci, V. Romano, G. Brunetti, N. Yaghoobi Nia, A. Di Carlo, G. D'Angelo, C. Ciminelli, Solar energy in space applications: review and technology perspectives, Adv. Energy Mater. 12 (2022) 2200125.
[2] G. Zhao, D. Hughes, D. Beynon, Z. Wei, T. Watson, W.T. Chung, J. Baker, Perovskite photovoltaics for aerospace applications– life cycle assessment and cost analysis, Solar Energy 274 (2024) 112602.
[3] Y. Tu, J. Wu, G. Xu, X. Yang, R. Cai, Q. Gong, R. Zhu, W. Huang, Perovskite solar cells for space applications: progress and challenges, Advanced Materials 33 (2021) 2006545.
[4] G. Xu, P. Cai, Y. Tu, H. Kong, Z. Ke, Y. Li, C. Zhuang, X. Du, Y. Zhang, Z. Li, Calibration for Space Solar Cells: progress, Prospects, and Challenges, Sol. RRL. 8 (2024) 2300822.
[5] M. Peciak, W. Skarka, K. Mateja, M. Gude, Impact analysis of solar cells on vertical take-off and landing (VTOL) fixed-wing UAV, Aerospace 10 (2023) 247.
[6] S. Tepner, A. Lorenz, Printing technologies for silicon solar cell metallization: a comprehensive review, Progress in Photovoltaics: Research and Applications 31 (2023) 557–590.
[7] M. Di Sabatino, R. Hendawi, A.S. Garcia, Silicon Solar Cells: trends, Manufacturing Challenges, and AI Perspectives, Crystals. (Basel) 14 (2024) 167.
[8] X. Wang, L. Xu, S. Ge, S.Y. Foong, R.K. Liew, W.W.F. Chong, M. Verma, M. Naushad, Y.-K. Park, S.S. Lam, Biomass-based carbon quantum dots for polycrystalline silicon solar cells with enhanced photovoltaic performance, Energy 274 (2023) 127354.
[9] J. Yu, Y. Chen, J. He, Y. Bai, R. Su, T. Cao, W. Liu, T. Chen, Enhancing poly-Si contact through a highly conductive and ultra-thin TiN layer for high-efficiency passivating contact silicon solar cells, Solar Energy Materials and Solar Cells 260 (2023) 112491.
[10] P. Panagiotou, I. Tsavlidis, K. Yakinthos, Conceptual design of a hybrid solar MALE UAV, Aerosp. Sci. Technol. 53 (2016) 207–219.
[11] L. Wang, J. Liu, Y. Li, G. Wei, Q. Li, Z. Fan, H. Liu, Y. An, C. Liu, J. Li, Dislocations in Crystalline Silicon Solar Cells, Advanced Energy and Sustainability Research 5 (2024) 2300240.
[12] J. Li, Q. Kang, Y. Wang, Z. Zhou, Z. Sun, H. Zhang, W. Lu, X. Tao, S. Zhang, X. Chen, Low oxygen content MoOx and SiOx tunnel layer based heterocontacts for efficient and stable crystalline silicon solar cells approaching 22% efficiency, Adv. Funct. Mater. 34 (2024) 2310619.
[13] A.B.G. Trabelsi, G.V. Kaliyannan, R. Gunasekaran, R. Rathanasamy, S. K. Palaniappan, F.H. Alkallas, W. Elsharkawy, A.M. Mostafa, Surface engineering of Sio2-Zro2 films for augmenting power conversion efficiency performance of silicon solar cells, J. Mater. Res. Technol. 28 (2024) 1475–1482.
[14] H. Lin, G. Wang, Q. Su, C. Han, C. Xue, S. Yin, L. Fang, X. Xu, P. Gao, Unveiling the mechanism of attaining high fill factor in silicon solar cells, Progress in Photovoltaics: Research and Applications 32 (2024) 359–371.
[15] Y. Li, Z. Chen, R. Zhou, W. Zhao, M. Li, J. Chen, Z. Huang, J. Liu, Y. Li, M. Yang, Design of advanced porous silver powder with high-sintering activity to improve silicon solar cells, Nano Res. 17 (2024) 3189–3197.
[16] L. Zhang, J. Qiu, H. Cheng, Y. Zhang, S. Zhong, L. Shi, H. Yin, R. Tong, Z. Sun, W. Shen, Low-temperature Ta-doped TiOx electron-selective contacts for high-performance silicon solar cells, Solar Energy Materials and Solar Cells 266 (2024) 112703.
[17] M. Janghorban, A. Tounsi, Two models for wave propagation in polymer/halloysite nanotube nanocomposites: network phenomena/generalized continuum mechanics, Waves in Random and Complex Media (2024) 1–32.
[18] S. Al-Houri, M.A. Al-Osta, F. Bourada, Q. Gawah, A. Tounsi, S.U. Al-Dulaijan, Analysis of Porosity-Dependent Wave Propagation in FG-CNTRC Beams Utilizing an Integral Higher-Order Shear Deformation Theory, International Journal of Structural Stability and Dynamics (2024) 2550233.
[19] A. Tounsi, S.I. Tahir, I.M. Mudhaffar, M.A. Al-Osta, A. Chikh, On the wave propagation characteristics of functionally graded porous shells, HCMCOU Journal of Science–Advances in Computational Structures (2024).
[20] Q. Gawah, F. Bourada, M.A. Al-Osta, S.I. Tahir, A. Tounsi, M. Yaylacı, An improved first-order shear deformation theory for wave propagation analysis in FG-CNTRC beams resting on a viscoelastic substrate, (2024).
[21] Y.-W. Zhang, H.-X. Ding, G.-L. She, A. Tounsi, Wave propagation of CNTRC beams resting on elastic foundation based on various higher-order beam theories, Geomechanics and Engineering 33 (2023) 381–391.
[22] S.I. Tahir, A. Tounsi, A. Chikh, M.A. Al-Osta, S.U. Al-Dulaijan, M.M. Al-Zahrani, The effect of three-variable viscoelastic foundation on the wave propagation in functionally graded sandwich plates via a simple quasi-3D HSDT, Steel and Composite Structures 42 (2022) 501.
[23] H. Fourn, H.A. Atmane, M. Bourada, A.A. Bousahla, A. Tounsi, S.R. Mahmoud, A novel four variable refined plate theory for wave propagation in functionally graded material plates, Steel and Composite Structures, An International Journal 27 (2018) 109–122.
[24] F. Bounouara, S.M. Aldosari, A. Chikh, A. Kaci, A.A. Bousahla, F. Bourada, A. Tounsi, K.H. Benrahou, H. Albalawi, The effect of visco-Pasternak foundation on the free vibration behavior of exponentially graded sandwich plates with various boundary conditions, Steel and Composite Structures, An International Journal 46 (2023) 367–383.
[25] R. Bennai, H.A. Atmane, A. Tounsi, A new higher-order shear and normal deformation theory for functionally graded sandwich beams, Steel and Composite Structures 19 (2015) 521–546.
[26] R. Bennai, R.A. Atmane, F. Bernard, M. Nebab, N. Mahmoudi, H.A. Atmane, S. M. Aldosari, A. Tounsi, Study on stability and free vibration behavior of porous FGM beams, Steel and Composite Structures, An International Journal 45 (2022) 67–82.
[27] E. Samaniego, C. Anitescu, S. Goswami, V.M. Nguyen-Thanh, H. Guo, K. Hamdia, X. Zhuang, T. Rabczuk, An energy approach to the solution of partial differential equations in computational mechanics via machine learning: concepts, implementation and applications, Comput. Methods Appl. Mech. Eng. 362 (2020) 112790.
[28] C. Anitescu, B. İsmail Ateş, T. Rabczuk, Physics-informed neural networks: theory and applications. Machine Learning in Modeling and Simulation: Methods and Applications, Springer, 2023, pp. 179–218.
[29] A. Ahmed, M.N. Uddin, M. Akbar, R. Salih, M.A. Khan, H. Bisheh, T. Rabczuk, Prediction of shear behavior of glass FRP bars-reinforced ultra-highperformance concrete I-shaped beams using machine learning, Int. J. Mech. Mater. Des. (2023) 1–22.
[30] B. Liu, W. Lu, T. Olofsson, X. Zhuang, T. Rabczuk, Stochastic interpretable machine learning based multiscale modeling in thermal conductivity of Polymeric graphene-enhanced composites, Compos. Struct. 327 (2024) 117601.
[31] B. Mortazavi, X. Zhuang, T. Rabczuk, A.V. Shapeev, Atomistic modeling of the mechanical properties: the rise of machine learning interatomic potentials, Mater. Horiz. 10 (2023) 1956–1968.
[32] B. Mortazavi, F. Shojaei, M. Shahrokhi, T. Rabczuk, A.V. Shapeev, X. Zhuang, Electronic, Optical, Mechanical and Li-Ion Storage Properties of Novel Benzotrithiophene-Based Graphdiyne Monolayers Explored by First Principles and Machine Learning, Batteries. (Basel) 8 (2022) 194.
[33] B. Liu, N. Vu-Bac, X. Zhuang, X. Fu, T. Rabczuk, Stochastic integrated machine learning based multiscale approach for the prediction of the thermal conductivity in carbon nanotube reinforced polymeric composites, Compos. Sci. Technol. 224 (2022) 109425.
[34] M. Safarpour, A. Rahimi, A. Alibeigloo, H. Bisheh, A. Forooghi, Parametric study of three-dimensional bending and frequency of FG-GPLRC porous circular and annular plates on different boundary conditions, Mechanics Based Design of Structures and Machines (2019) 1–31.
[35] Y. Wang, R. Zeng, M. Safarpour, Vibration analysis of FG-GPLRC annular plate in a thermal environment, Mechanics Based Design of Structures and Machines (2020) 1–19.
[36] A. Rahimi, A. Alibeigloo, High-Accuracy Approach for Thermomechanical Vibration Analysis of FG-Gplrc Fluid-Conveying Viscoelastic Thick Cylindrical Shell, Int. J. Appl. Mechanics 12 (2020) 2050073, https://doi.org/10.1142/S1758825120500738.
[37] S.R. Wenham, M.A. Green, Silicon solar cells, Progress in Photovoltaics: Research and Applications 4 (1996) 3–33.

[38] J.N. Reddy, Mechanics of Laminated Composite Plates and shells: Theory and Analysis, CRC press, 2003.
[39] B. Akgöz, Ö. Civalek, A microstructure-dependent sinusoidal plate model based on the strain gradient elasticity theory, Acta Mech. 226 (2015) 2277–2294.
[40] C. Zhu, X. Fang, J. Liu, Relationship between nonlinear free vibration behavior and nonlinear forced vibration behavior of viscoelastic plates, Communications in Nonlinear Science and Numerical Simulation 117 (2023) 106926, https://doi.org/10.1016/j.cnsns.2022.106926.
[41] S.I. Tahir, A. Tounsi, A. Chikh, M.A. Al-Osta, S.U. Al-Dulaijan, M.M. Al-Zahrani, An integral four-variable hyperbolic HSDT for the wave propagation investigation of a ceramic-metal FGM plate with various porosity distributions resting on a viscoelastic foundation, Waves in Random and Complex Media 34 (2024) 1616–1639.
[42] Y. Qiu, Y., and J. Wang, "A Machine Learning Approach to Credit Card Customer Segmentation for Economic Stability." In Proceedings of the 4th International Conference on Economic Management and Big Data Applications, ICEMBDA 2023, October 27–29, 2023, Tianjin, China. 2024.